UNIVERSITAT POLITÈCNICA DE VALÈNCIA

Escuela Técnica Superior de Ingeniería del Diseño

UNIVERSITAT POLITÈCNICA DE VALÈNCIA

School of Aerospace Engineering and Industrial Design

1D Simulations for Understanding Biphasic Blood Flow in Simple Capillary Occlusions

Master's Thesis

Master's Degree in Computational Fluid Dynamics

AUTHOR: Tejeda Chas, Javier

Tutor: Sánchez Anguix, Víctor

External cotutor: SCHMID, FRANCA

ACADEMIC YEAR: 2023/2024

Abstract

In the complex realm of brain health, cortical microinfarcts emerge as subtle yet powerful factors, closely linked to conditions like cerebral amyloid angiopathy and dementia [24, 25, 13, 22]. Despite their significant impact on disease progression, detecting these microinfarcts is often challenging, as their influence remains concealed within the blood circulation in the brain's capillary networks.

Microstrokes, the culprits responsible for these microinfarcts, occur when small blood vessels or capillaries in the brain face blockages, triggering local disturbances in the surrounding tissue. While each microstroke may not cause substantial damage on its own, their cumulative effect poses an increased risk of conditions such as dementia, including Alzheimer's disease.

The brain's limited energy storage emphasizes the crucial need for a continuous supply of oxygen and nutrients to prevent local tissue damage. Even at the level of individual vessels, microinfarcts can lead to lesions in cortical tissue, highlighting the importance of understanding their role in local blood supply dynamics.

Animal models, utilized by employing methods that involve blocking blood vessels, provide a detailed perspective into the origins of microinfarcts. However, the focus on penetrating vessels has left occlusions of descending arteriole offshoots and capillaries relatively unexplored, and herein lies a crucial aspect of our investigation.

In this study, we delve into the often-overlooked domain of microstrokes and their impact on brain blood flow. Through simulations in realistic microvascular networks from the mouse cortex, we analyze the effects of single-capillary blockages, revealing a nuanced interplay between local vascular structure and baseline flow rates. The simulations are based in the resolution of an inverse problem in which the boundary conditions pressure are tuned, which is one of the key challenges related to modeling blood flow in realisitic microvascular networks.

Our research aims to bridge the understanding gap regarding the distribution of cortical blood flow in both healthy and ischemic stroke scenarios, since it was demonstrated that microstroke disturbs blood flow locally [16, 17, 19]. Through in silico simulations in a microvascular network from the mouse cortex [3], the aim is to compare healthy conditions with those during occlusion to demonstrate results that cannot be captured experimentally.

This master thesis was executed at the ARTORG Center for Biomedical Engineering Research (University of Bern, Switzerland) during the period from 01/08/2023 to 31/01/2024. The stay at the center was supervised and jointly supervised by Dr. Franca Schmid and Chryso Lambride during the study.

Resumen

En el complejo ámbito de la salud cerebral, los microinfartos corticales emergen como factores importantes, estrechamente vinculados a condiciones como la angiopatía amiloide cerebral y la demencia [24, 25, 13, 22]. A pesar de su impacto significativo en la progresión de la enfermedad, detectar estos microinfartos suele ser un desafío, ya que su influencia permanece oculta dentro de la circulación sanguínea en las redes capilares del cerebro.

Los microictus, responsables de estos microinfartos, ocurren cuando pequeños vasos sanguíneos o capilares en el cerebro se bloquean, desencadenando alteraciones locales en el tejido circundante. Aunque cada microictus puede no causar daños sustanciales por sí solo, su efecto acumulativo plantea un riesgo aumentado de condiciones como la demencia, incluyendo la enfermedad de Alzheimer.

El almacenamiento de energía limitado del cerebro destaca la necesidad crucial de un suministro continuo de oxígeno y nutrientes para prevenir daños en el tejido local. Incluso a nivel de vasos individuales, los microinfartos pueden provocar lesiones en el tejido cortical, resaltando la importancia de comprender su papel en la dinámica del suministro sanguíneo local.

Los modelos animales, utilizados empleando métodos que implican el bloqueo de vasos sanguíneos, proporcionan una perspectiva detallada sobre los orígenes de los microinfartos. Sin embargo, el enfoque en los vasos penetrantes ha dejado las oclusiones de las ramificaciones arteriolares descendentes y los capilares relativamente inexploradas, y aquí radica un aspecto crucial de nuestra investigación.

En este estudio, nos adentramos en el dominio a menudo pasado por alto de los microictus y su impacto en el flujo sanguíneo cerebral. A través de simulaciones en redes microvasculares realistas del córtex de ratón, analizamos los efectos de los bloqueos de capilares individuales, revelando una interacción compleja entre la estructura vascular local y los valores de flujo antes del bloqueo. Las simulaciones se basan en la resolución de un problema inverso en el cual se ajustan las condiciones de presión de contorno, que es uno de los desafíos clave relacionados con la modelización del flujo sanguíneo en redes microvasculares realistas.

Nuestra investigación tiene como objetivo cerrar la brecha de entendimiento con respecto a la distribución del flujo sanguíneo cortical en escenarios tanto sanos como de accidente cerebrovascular isquémico, ya que se demostró que el microictus perturba el flujo sanguíneo localmente [16, 17, 19]. A través de simulaciones in silico en una red microvascular del córtex de ratón [3], el objetivo es comparar las condiciones saludables con aquellas durante la oclusión para demostrar resultados que no pueden ser capturados experimentalmente.

Este Trabajo de Fin de Máster se realizó en ARTORG Center for Biomedical Engineering Research (Universidad de Berna, Suiza) durante el período del 01/08/2023 al 31/01/2024. La estancia del alumno en el centro fue supervisada conjuntamente por la Dra. Franca Schmid y Chryso Lambride.

Contents

List of Tables

List of Figures

Abbreviations

RBC - Red Blood Cell
WBC - White Blood Cell
CoW - Circle of Willis
MCA - Middle Cerebral Artery
ACA - Anterior Cerebral Artery
PCA - Posterior Cerebral Artery
PA - Pial Artery
PV - Pial Vein
DA - Descending Artery
AV - Ascending Vein
CBF - Cerebral Blood Flow
SMC - Smooth Muscle Cells
SMA - Smooth Muscle Actin
Re - Reynolds number
Wo - Womersley number
De - Dean number
CFL - Cell Free Layer

1. Introduction

This section aims to elucidate the study's motivation, outline the objectives to be achieved, and describe the contributions made towards reaching these goals. It also contextualizes related studies to date and provides a brief overview of the document's structure.

This study focuses on simulations of microvascular networks under healthy conditions and with the blockage of a capillary in the network to better understand how these occlusions affect flow locally and globally for comparison with healthy conditions.

1.1 Motivation

According to the World Health Organization, dementia affects over 55 million people worldwide, with 60% living in low and middle-income countries. Each year sees nearly 10 million new cases. This condition, which primarily impacts those over 65, is mainly driven by Alzheimer's disease, representing 60–70% of cases. Dementia leads to memory, cognition, and daily function decline, often accompanied by mood, behavior, and motivational changes, and is the seventh leading cause of death globally. Its progression is marked by a variety of diseases and injuries that progressively damage the brain. The syndrome not only causes considerable physical, psychological, social, and economic consequences for individuals and caregivers but also poses significant challenges in diagnosis and care access, highlighting the critical need for increased awareness and support.

Microinfarcts are blockages of small blood vessels, including capillaries in the brain. These occlusions have no visible or significant impact at the time. However, research has shown that their accumulation increases the risk of developing dementia [24, 25, 13, 22, 21].

The brain, much like any other organ, depends on oxygenated blood, which originates in the lungs and is distributed to all tissues throughout the body via an intricate network of blood vessels. Despite its relatively modest size and a weight of approximately 1 kg, the human brain accounts for about 20% [6] of the body's total oxygen supply, roughly equivalent to one liter of blood volume per minute. Ensuring a continuous and robust blood supply to all regions of the brain is imperative at all times, considering the limited energy storage capacities and the variable demands associated with fluctuations in neuronal activity.

In contrast to major strokes affecting large blood vessels, microstrokes are exceedingly challenging to detect. This lack of detectability, despite their association with future diseases such as dementia or Alzheimer's, has resulted in limited investigation into their impact and prevalence. While microstrokes do not inflict the extensive damage characteristic of major strokes, the accumulation of numerous microstrokes over time can contribute to the development of the aforementioned diseases in the future.

1.2 Objectives

Two concepts are fundamental to explaining the goals of this work, as they are vital to it.

The boundary conditions are a set of constraints which represent the border of a domain. In

this study, they represent pressure constraints in the border of the network, i.e., the inflows and outflows of our system.

For its part, an inverse problem involves achieving certain physical measurements, for example, experimentally measured velocities, by altering another parameter or other parameters after having calculated the relationship between the physical measurements and the parameters.

The present in silico study aims to tune the boundary conditions by solving an inverse problem, using the Gradient Descent algorithm, to investigate single capillary occlusions in a real capillary network. This network is extracted from the brain of a mouse using in vivo two-photo imaging. Experimental data pertaining to red blood cell (RBC) velocities within distinct vessels of the vascular network were acquired by collaborators at the Institute of pharmacology and toxicology at the University of Zurich (group of prof. Bruno Weber). Furthermore, the occlusion of a specific blood vessel will be induced, followed by subsequent velocity measurements at various time intervals post-stroke induction. This methodology aims to elucidate the temporal duration of the vascular occlusion effect and, consequently, the duration required for complete restoration of blood flow to pre-occlusion levels.

These velocity measurements will reduce uncertainty in flow simulations. In essence, the inverse problem will be addressed by obtaining a solution, amidst a broad spectrum of possibilities, for the pressure values of boundary conditions. In vivo velocities will be targets for solving the inverse problem. The solution depends on these targets, boundary condition initialization, learning rate, and other factors.

The objectives are as follows:

- Designing a computational framework consistent with in vivo observations to accurately simulate microstroke.
- Implementing a methodology that allows for accurately achieving the experimental measurements obtained, while obtaining a solution within the physiological ranges of RBC velocity, flow rate, network pressure difference, CBF. Given that a local minimum search algorithm like Gradient Descent is used, it is necessary to force the system to converge to a solution that meets these characteristics, as there are multiple solutions that, through changes in pressure in the boundary conditions, achieve the experimental measurements.
- Comparison of the obtained results between stroke and healthy conditions to better understand the consequences of a single capillary occlusion.

1.3 Work contributions

The simulations for this study were executed using MicroBlooM [1], which is a Python code to model microvascular flow (forward problem), including various inverse models to incorporate in vivo data.

[1] https://github.com/Franculino/microBlooM

Although experimental measurements help reduce the uncertainty of potential solutions to the problem, they alone are insufficient for accurately simulating microvascular physiological conditions. Therefore, the main contribution of this work is to develop a methodology that can simulate these physiological conditions while precisely achieving these experimental measurements. For this purpose, the cost function of the algorithm will be modified, with all subsequent changes necessary for the correct functioning of the algorithm.

Furthermore, this study conducts an analysis and comparison between healthy and occluded conditions to better understand how these blockages affect the system.

1.4 Document structure

The document is structured into various sections, starting with this brief introduction to the problem and the motivation for the study. This is followed by a theoretical framework that outlines the current understanding and knowledge surrounding cerebral microinfarcts and related topics. The subsequent section will detail the methodologies employed in the project's development. Finally, the document concludes with the presentation of the research findings and a discussion that evaluates and interprets the significance of these results.

2. Theoretical Framework

Before exploring this work, we must clarify basic aspects like blood vessel anatomy, the Circle of Willis (CoW), and related components. Knowing these basics sets the stage for detailed study of cortical microinfarcts and their significant impact on brain health.

Furthermore, it is equally important to understand the method underlying the simulations conducted. Therefore, this section elaborates on both the physiological context and all the necessary concepts to comprehend how the simulations presented later were performed.

2.1 Physiological context

Blood, a crucial and complex fluid, transports oxygen, nutrients, and waste products in the body. Understanding blood flow dynamics, especially in the capillary network, is key to uncovering the processes of circulatory systems.

2.1.1 Blood composition, rheology and viscosity

Blood is composed of distinct elements, each playing a pivotal role in maintaining homeostasis, i.e., the process through which organisms regulate themselves to maintain necessary conditions and achieve equilibrium. Blood plasma, constituting approximately 55% [6], is a yellowish aqueous liquid exhibiting dynamic viscosity (μ) of 0.0012 Pa s. This Newtonian, homogeneous, and incompressible fluid transports various substances, from ions to large proteins, facilitating the movement of nutrients and waste products.

The remaining 45% comprises cellular elements [6], primarily RBCs, White Blood Cells (WBCs), Platelets, and others. RBCs are disc-shaped and flexible, and transport oxygen to tissues. Their deformability allows passage through capillaries with diameters less than 4μm. White Blood Cells, constituting less than 1% and form a vital part of the immune system. Platelets represent also less than 1% and contribute to blood coagulation [6].

Blood viscosity varies across vessel sizes. In large vessels, blood behaves as a Newtonian fluid with dynamic viscosity (μ) ranging from 0.0035 to 0.0045 Pa·s [23]. In small vessels, non-Newtonian behavior emerges, influenced by temperature, shear rate, vessel diameter, and haematocrit. These characteristics must be considered when modeling blood flow, as the simulation approach varies between microvasculature and larger veins and arteries.

The apparent viscosity (μ_a) derived from Poiseuille's law increases with haematocrit [15]. Blood exhibits shear-thinning properties, with viscosity decreasing at higher shear rates. This phenomenon, coupled with RBC aggregation, influences blood's rheological behavior, particularly in microvascular networks.

Haematocrit is the ratio of RBC volume to total blood volume and it plays a pivotal role in determining blood viscosity. Under laminar flow conditions, higher haematocrit levels lead to increased blood viscosity due to the disturbance of flow streamlines by cellular elements [15]. This disruption is particularly pronounced in smaller vessels, impacting microcirculation. Alterations in haematocrit, a dynamic parameter influenced by various physiological and

pathophysiological processes, can significantly affect blood viscosity and, consequently, tissue perfusion.

RBC deformability is another crucial factor influencing blood flow. Deformable RBCs easily orient themselves in flow streamlines, reducing viscosity, especially in large blood vessels (the order of magnitude of their diameter varies from cm to mm) due to the Fahraeus-Lindqvist effect [14, 9]. In smaller vessels (μm), RBC deformability affects this effect, contributing to a deformability-related reduction in flow resistance and an increased viscosity [14]. The unique biconcave discoid shape of RBCs allows for reversible deformations, responding to applied forces as elastic and viscous bodies. This deformability is influenced by factors such as cytoplasmic viscosity, membrane properties, and the concentration of hemoglobin. Furthermore, RBCs have a tendency to aggregate into linear arrays or rouleaux, a phenomenon influenced by plasma protein composition and RBC surface properties. However, capillaries are generally too small to see these rouleaux.

RBC aggregation is the tendency of RBCs to form clusters or rouleaux in the bloodstream [2]. This process, influenced by factors like shear forces and plasma proteins, plays a crucial role in blood rheology. In areas of low shear, such as the microcirculation, RBCs tend to form larger aggregates, impacting blood fluidity and increasing apparent viscosity. Various factors, including changes in plasma protein composition and alterations in RBC surface properties, can modulate the degree of aggregation. Understanding RBC aggregation is essential for comprehending blood flow dynamics and its implications for tissue perfusion.

2.1.2 Brain vasculature

In this chapter, a comprehensive exploration of the vascular anatomy of the brain is undertaken, shedding light on crucial components such as the Circle of Willis, cortical vasculature, and the fundamental aspects of blood flow regulation.

The blood supply to the brain commences through the vertebral and internal carotid arteries, culminating in the formation of the Circle of Willis. This circulatory anastomosis among the main cerebral arteries—middle cerebral artery (MCA), anterior cerebral artery (ACA), and posterior cerebral artery (PCA)—is pivotal for reinforcing cerebral blood supply. The CoW strategically provides alternative flow paths, mitigating the impact of potential blockages or narrowing in the feeding arteries.

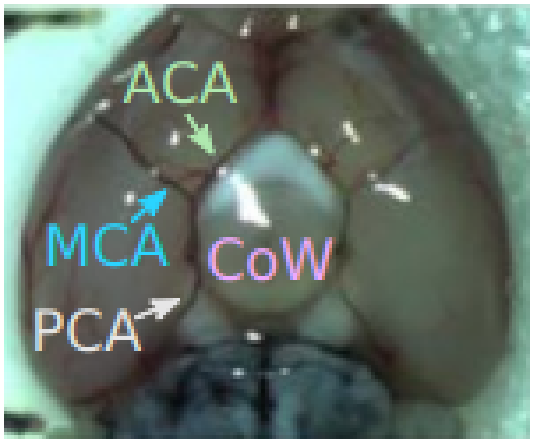

Figure 1: Mouse brain from below showing the CoW and the cerebral arteries. Figure from: [6]

Turning attention to the cerebral cortex, the outermost layer of neural tissue, a planar network of interconnected pial arteries (PAs) receives blood from the main cerebral arteries [8]. Anastomoses between different branches of PAs enhance redundancy, ensuring resilience to single vessel obstructions. Descending arteries (DAs) impregnate the brain, supplying various cortical layers, and their terminal ends connect to a highly interconnected capillary network responsible for the essential exchange of oxygen, nutrients and wastes.

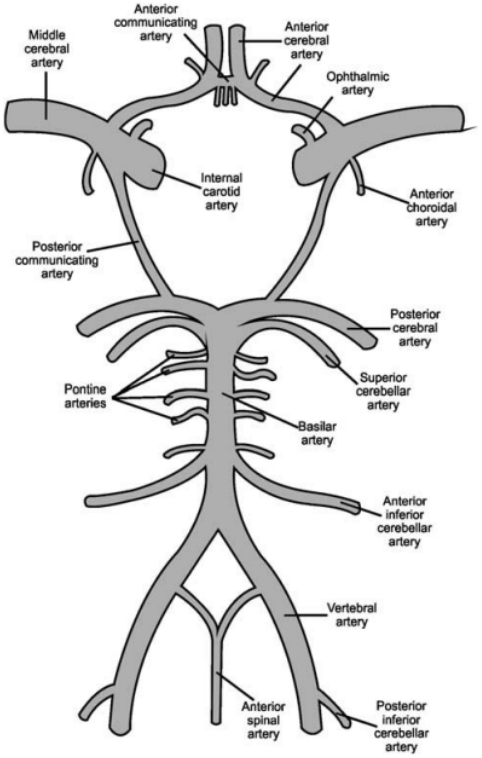

Figure 2: Principal components of the Circle of Willis. Figure from: [26]

The resulting deoxygenated blood is then collected and directed through the ascending venules (AVs), depicted in blue in Figure 3, which lead to the Pial Veins (PVs).

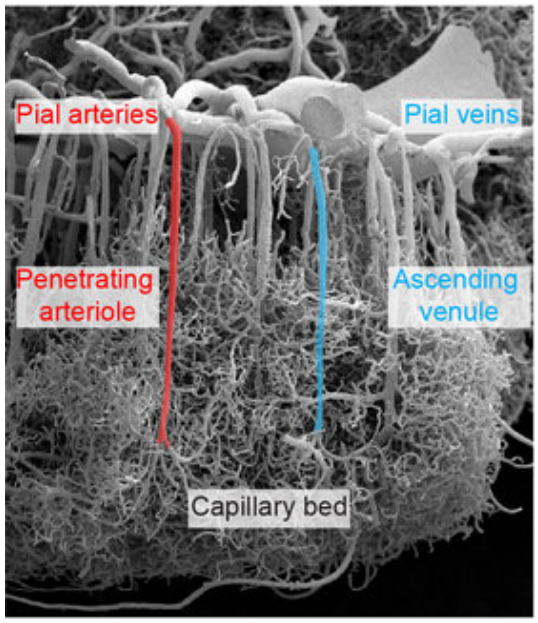

Figure 3: Scanning electron microscopy image. Figure from: [4]

An important parameter to be taken into account is the Cerebral Blood Flow (CBF). It refers to the amount of blood that flows through the brain's blood vessels in a given amount of time. It is an important parameter because it plays a crucial role in maintaining normal brain function. Changes in CBF can indicate various brain conditions, such as brain injury, stroke, or epilepsy. Monitoring CBF can help diagnose and manage these conditions, as well as guide treatment decisions.

2.1.3 Blood flow regulation

The brain's vasculature possesses a remarkable capability to finely adjust blood supply in response to localized neuronal activity, a phenomenon known as neurovascular coupling, with roots dating back over a century. Despite its longstanding recognition, the precise signaling pathways orchestrating the communication between neurons, astrocytes, and the vasculature, as well as the detailed dynamics of vascular diameter changes, remain subjects of ongoing exploration.

Smooth muscle cells (SMCs) and pericytes stand out as influential regulators of blood vessel diameters [8, 28], as depicted in Figure 4. Enriched in α-smooth muscle actin (α-SMA), SMCs encircle PAs and DAs [6]. Simultaneously, pericytes, also expressing α-SMA, strategically position themselves in the transition zone between DAs and capillaries [28]. It is known that SMCs and pericytes exert the control over vascular diameters [28], underscoring their pivotal role in blood flow regulation. The dynamic adjustments in blood supply, orchestrated by these mural cell types, respond to the intricate interplay between neurons, astrocytes, and the vasculature, shaping the landscape of active research in this domain.

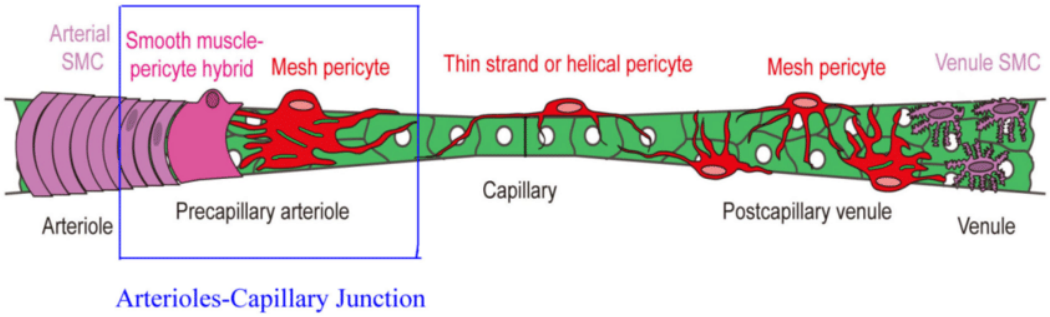

Figure 4: SMCs and perycites in the brain microvasculature. Figure from: [28]

2.1.4 Ischaemic strokes, microstrokes and collateral circulation

Stroke, impacting 13.7 million people annually [6], is a major global health concern leading to death and disability. The prevalent subtype, ischemic stroke, results from a blood clot obstructing a major feeding artery, causing a severe reduction in downstream blood flow. Without timely intervention, the affected brain region experiences insufficient oxygen and nutrient supply, ultimately leading to neuronal cell death. Treatment urgency is emphasized, focusing on clot removal through thrombolysis or mechanical thrombectomy. Collateral circulation plays a vital role during this critical period, acting as a lifeline by sustaining a residual blood supply to the under-supplied brain region. The Circle of Willis serves as a primary route for collateral flow, offering redundant blood supply, but limitations arise when vessel occlusions occur distal to it, particularly in the middle cerebral artery. Leptomeningeal collaterals become crucial in these scenarios [6], connecting downstream branches and significantly influencing the potential for delaying or preventing cell death after a stroke. Robust collateral circulation enhances the success rate of stroke treatments.

Now, shifting our focus to microstrokes—a phenomenon involving the blockage of tiny blood vessels or capillaries in the brain—it's crucial to note that while microstrokes do not cause the same level of damage as major strokes, they do elevate the risk of developing conditions like dementia, including Alzheimer's disease, later in life [19]. Individuals with these neurodegenerative conditions often exhibit a reduced capillary count in their brains. Capillaries create a intricate network supplying the majority of energy and oxygen to the brain. Repeated microstrokes may contribute to a progressive loss of capillaries over time, potentially exacerbating memory loss and other cognitive difficulties.

2.2 Modeling flow in small blood vessels

In this section, the fundamental principles governing the modeling of blood flow in small blood vessels are discussed, with a specific focus on PAs, DAs, capillaries, AVs, and PVs within the microvasculature. First, the Navier-Stokes equations are presented along with the simplifications assumed in them, including an explanation of the dimensionless numbers

that ensure these simplifications can be made. Additionally, the incorporation of red blood cells into the simulations is explained, as well as effects occurring in the microcirculation that need to be considered.

2.2.1 Governing equations

In the first instance, we start with the fundamental assumption that blood behaves as an incompressible Newtonian fluid. Consequently, it is considered to have a constant density ρ and dynamic viscosity μ. This assumption simplifies the modeling approach and is grounded in the understanding that, within the scope of the analysis, the blood's response to shear forces is linear.

In fluid dynamics, dimensionless numbers play a crucial role in understanding and elucidating flow characteristics. Two commonly employed dimensionless numbers in the study of blood flow through small blood vessels are the Reynolds number (Re) and the Womersley number (Wo) [6].

The Reynolds number signifies the ratio of inertial forces to viscous forces in a fluid system. For blood flow in small vessels, it is calculated using the formula:

$$Re = \frac{\rho \cdot V^{char} \cdot D^{char}}{\mu} \tag{1}$$

where ρ is the blood density, V^{char} is the blood flow velocity, D^{char} is the characteristic diameter of the vessel, and μ is the dynamic viscosity of blood.

The Womersley number is pertinent in the context of pulsatile flow, often encountered in blood circulation. It is defined as:

$$Wo = \frac{D^{char}}{2} \cdot \sqrt{\frac{\omega^{char} \cdot \rho}{\mu}} \tag{2}$$

where ω^{char} is the angular frequency of pulsatile flow, ρ is the blood density, μ is the dynamic viscosity of blood.

Meanwhile, the Dean number (De) [5] is an additional dimensionless parameter that characterizes the balance between inertial and centripetal forces relative to viscous forces in a flowing system. Unlike the Reynolds number (Re) and the Womersley number (Wo), as previously discussed, the Dean number specifically considers the effects of curvature in a vessel. Mathematically, it is expressed as:

$$De = \frac{Re \cdot \frac{d_{\text{char}}}{2}}{r_c} \quad (3.8) \tag{3}$$

Here, r_c signifies the curvature radius of the vessel. The Dean number essentially quantifies the competition between the tendency of fluid particles to move in a straight line (inertia) and the centripetal forces that arise due to vessel curvature, in relation to the resistance offered by viscosity.

In the context of our study on blood flow through small vessels, such as capillaries, it's important to note that the Reynolds, Womersley, and Dean numbers collectively provide a comprehensive understanding of the fluid dynamical flow regime. However, for cases where the Dean number is considerably small ($De < 1$), as is often the scenario in microvasculature, the secondary flow phenomena induced by vessel curvature can be safely disregarded. This allows for the continued validity of the assumption of straight blood vessels, simplifying the modeling approach.

In the small blood vessels considered in this study, both the Reynolds and Womersley numbers consistently exhibit values below 1. This implies that viscous forces significantly outweigh inertial forces and pulsatile effects. The consistently small values of these dimensionless numbers suggest that the blood flow within these vessels is characterized by laminar regime, i.e., a flow that is non-turbulent and without significant irregularities.

Using standard notation, the dynamics of blood flow is described by the Navier-Stokes equations, i.e.,

$$\boldsymbol{\nabla} \cdot \mathbf{u} = 0 \tag{4}$$

and

$$\rho \frac{\partial \mathbf{u}}{\partial t} + \rho(\mathbf{u} \cdot \boldsymbol{\nabla})\mathbf{u} = -\boldsymbol{\nabla} p + \mu \boldsymbol{\nabla}^2 \mathbf{u} \tag{5}$$

where $\mathbf{u}$, p, and t are the velocity vector, pressure, and time, respectively, and $\boldsymbol{\nabla}$ is the del-operator. Note that the two equations account for the conservation of mass, Eq. 4, and momentum, Eq. 5.

Now, due to the small values of the Reynolds and Womersley numbers, it indicates that the flow is dominated by viscosity. In other words, viscous forces are much stronger than inertial forces. Therefore, inertial and unsteady effects can be neglected. Eq. 5 simplifies to the Stokes equation described in Eq. 6:

$$\mu \boldsymbol{\nabla}^2 \mathbf{u} - \boldsymbol{\nabla} p = 0 \tag{6}$$

Continuing from the assumptions of incompressible Newtonian fluid behavior, the velocity profile in a straight blood vessel of constant diameter d can be derived based on the Hagen-Poiseuille model. Starting with Eqs. 4 and 6, the axial flow velocity ($u_z(r)$) as a function of the radial distance (r) to the vessel axis (z-axis) is expressed as follows:

$$u_z(r) = \frac{r^2 - \left(\frac{d}{2}\right)^2}{4\mu} \frac{dp}{dz} \tag{7}$$

Where $\frac{dp}{dz}$ denotes the pressure gradient. In the case of a fully developed flow, where the velocity profile achieves a stable state, $\frac{dp}{dz}$ remains constant and can be defined as the overall pressure decrease (Δp) across the vessel's length (l).

$$\frac{dp}{dz} = -\frac{\Delta p}{l} \tag{8}$$

Figure 5(a) provides an illustration of the parabolic velocity profile of plasma flow described by Eq. 7.

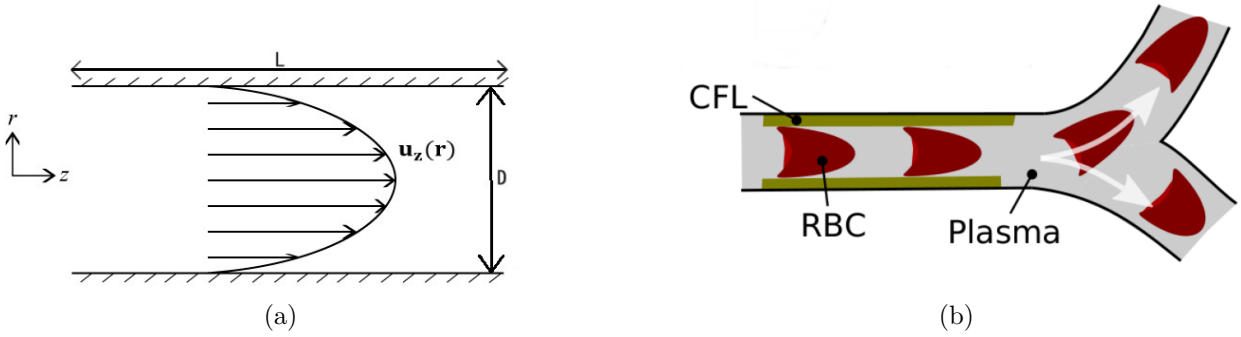

(a) (b)

Figure 5: (a) Parabolic velocity profile. (b) Scheme of a vessel showing the CFL and the RBCs circulating. Figure from: [6]

The flow rate (q) in the vessel is obtained by integrating Eq. 7 over the entire surface area:

$$q = \int_0^{d/2} u_z(r) 2\pi r dr = \frac{\pi d^4}{128 \mu l} \Delta p \tag{9}$$

This expression is commonly known as Poiseuille's law and provides a quantitative relationship between the flow rate, vessel diameter, pressure drop, and fluid viscosity.

These derivations showcase the characteristic parabolic velocity profile and the fundamental law governing blood flow through a straight vessel under the assumptions of incompressible Newtonian fluid behavior.

The derivation of Eq. 9 was based on the assumption that the vessel can be modeled as a straight pipe. This is consistent with what was explained before about the small Dean number we have in these small vessels. The secondary flow phenomena can be neglected by using straight vessels to simplify the calculations.

Returning to the Eq. 9, it was assumed that the flow is fully developed. The entrance of the vessels could be a problematic location as the velocity gradients and wall shear stresses are higher at this location. However, because we are in a situation where the Reynolds number is very small, and the radius is much smaller than the length of the vessels (4-10μm, for capillaries), it is reasonable to make this assumption over the entire length of the vessel.

2.2.2 RBC related flow phenomena

In the context of microcirculation, blood no longer behaves as a Newtonian fluid. Within this environment, additional flow phenomena occur. Mainly due to the presence of blood particles, especially RBCs, which represent a major part of blood (∼45%). However, cells such as white blood cells or platelets can be neglected as they constitute a very small part of the volume concentration of the blood (∼0.2%). Subsequently, we will delve into the

influence of red blood cells on microcirculation, exploring the implications associated with their presence.

As mentioned above, red blood cells are highly deformed cells. This allows them to pass through capillaries, here, with a parachute or slipper shape. Due to the limited space in the capillaries, the RBCs move in a single file, whereas in larger blood vessels several red blood cells pass through at the same time in a multi-row fashion.

The section close to the vessel wall is called the **cell-free layer** (CFL) [20, 10], as the red blood cells, in both cases, tend to detach from the vessel wall and move through the central part of the vessels. Using a velocity profile as in Eq. 7 the velocity in the centre of the vessels is higher, and this, together with the fact that the red blood cells travel through this area, means that they have a higher velocity than the bulk flow velocity. Due to the alignment of the RBCs in the capilaries, what is known as the **Fåhræus effect** is created. This means that the tube haematocrit (volume fraction of RBCs flowing in a tube), is lower than the discharged haematocrit (volume fraction of RBCs discharged in a reservoir).

The existence of the cell-free layer (CFL) and red blood cells substantially alters the flow dynamics, exerting a notable impact on vessel transmissibility. A more comprehensive description of the apparent relative viscosity will be provided in section 2.3.3; however, at present, it is encapsulated by the following definition:

$$T_{ij} = \frac{\pi d_{ij}^4}{128 l_{ij} \mu_p \mu_{rel,ij}} \tag{10}$$

Where l_{ij} and d_{ij} are the length and diameter of the respective vessel, μ_p is the plasma blood viscosity, and $\mu_{\text{rel},ij}$ is the relative apparent viscosity that is multiplied to each vessel to account for the RBC presence. This apparent viscosity depends on the tube haematocrit and the diameter of the vessel, and reaches its minimum value for a vessel diameter of $\approx 6\mu m$, as it can be seen in Figure 6a. This change in the viscosity is called the **Fåhræus-Linqdvist effect**.

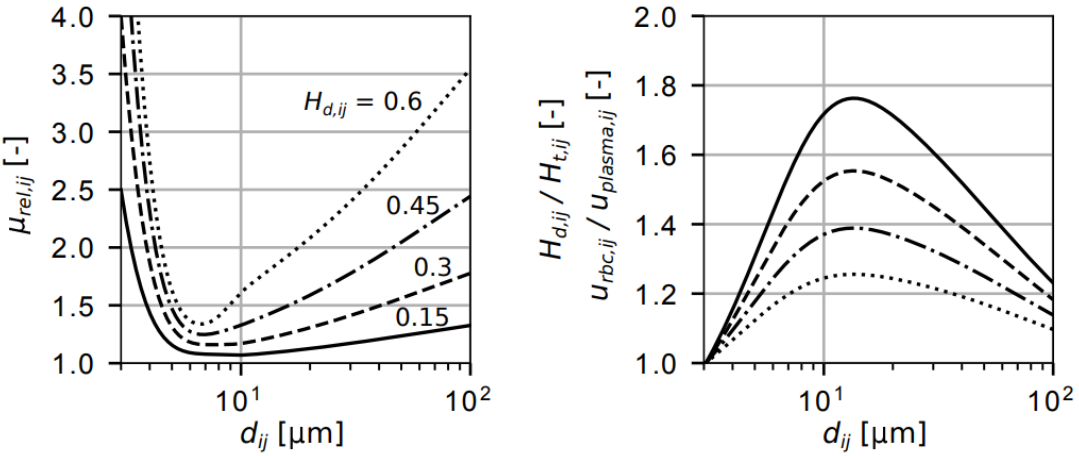

(a) (b)

Figure 6: Representations of the Fåhræus-Linqdvist and Fåhræus effects are depicted. Panel (a) illustrates the variation in the relative apparent viscosity, denoted as $\nu_{rel,ij}$, concerning vessel diameters and various discharge haematocrits. Meanwhile, panel (b) showcases the ratio of $u_{rbc,ij}$, to the mean plasma flow velocity, $u_{plasma,ij}$, across different vessel diameters and discharge haematocrits. Figure from:[6]

Another important factor to consider is the **phase-separation** at diverging bifurcations. This refers to how the red blood cells are distributed at diverging bifurcations. In general, when they go in single file in the microvasculature, more red blood cells tend to follow the higher local pressure gradient, and therefore a greater number of red blood cells will be directed towards the branch of the bifurcation with greater velocity. This also tends to happen in vessels with a larger diameter, where the branch with the higher velocity receives disproportionately more red blood cells than the other. It is important to note that there are empirical equations that describe this behaviour [15].

2.3 Forward problem

This problem directly solves the pressure field, contingent upon knowing the pressure at the boundary conditions for problem resolution. From these pressures, the flow rate, RBC velocities and pressure field, are computed for each blood vessel or node [16, 8].

2.3.1 Graph representation

The brain's microvasculature is formed by a dense network of interconnected blood vessels. In the models used in this work, each blood vessel is represented as a straight pipe with a constant diameter, mirroring the flow resistance and length of the corresponding real tortuous vessel. As explained in Section 2.2.1, this microvasculature presents small Reynolds, Womersley and Dean number, so we can safely make this assumption. This complex structure is effectively modeled as a network, comprising N_e, which represents the edge of each individual blood vessels and N_v vertices representing connections or intersections of two or

more blood vessels. The line that connects two vertices $v_i \in$ v and $v_j \in$ v is symbolized as $e_{ij} \in$ e, where v and e denote the sets of all vertices and edges of the network.

In order to represent the different characteristics or attributes of the vertex and edges of the network, the notation a_i is used to represent a vertex, and a_{ij} for the edges. Here, a represents the different attributes we have, as summarize in table 1.

Table 1: Vertex and Edge Attributes

Vertex attributes		**Edges attributes**	
Pressure	P	Diameter	d
Source/sink terms	b	Length	l
		Tube haematocrit	H_t
		Discharge haematocrit	H_d
		Relative apparent viscosity	μ_{rel}
		Transmissibility	T
		Flow rate	q
		Flow direction	dir
		Red blood cell velocity	u_{rbc}

In Figure 7 it can be seen a small part of the real tortuous network representation and the representation of the network considering vessels as straight pipes.

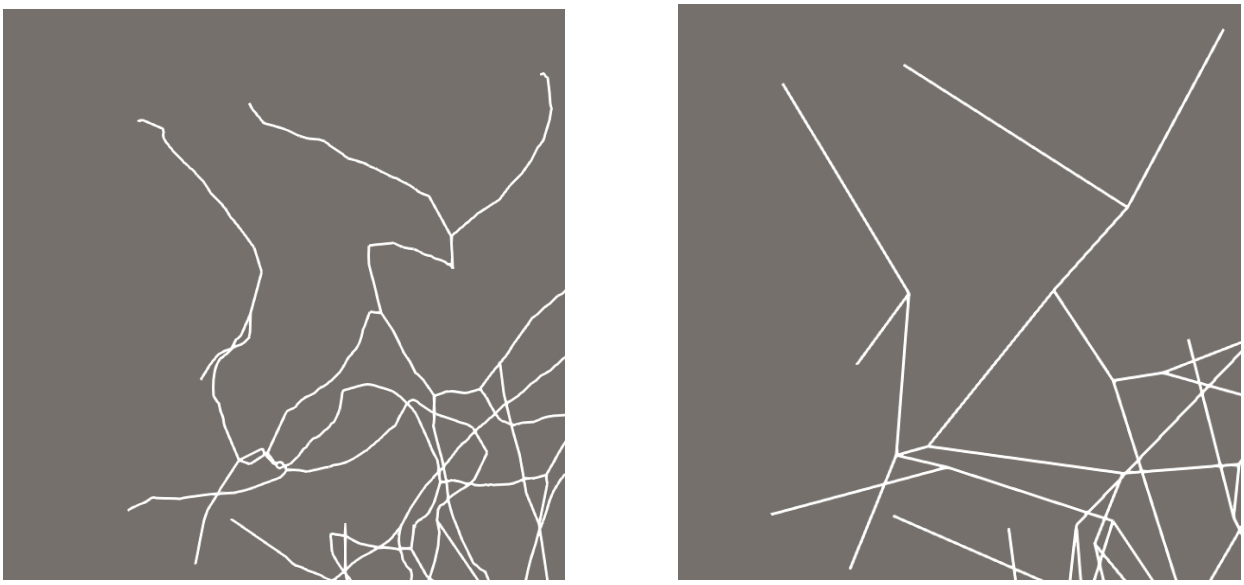

(a) (b)

Figure 7: (a) Tortuous representation of a realistic microvascular network (b) Corresponding network representing the vessels as straight pipes.

2.3.2 Solving the problem

As explained earlier, in this work, blood simulations are treated as biphasic, consisting of plasma and red blood cells. These simulations involve solving a linear system of equations comprising two fundamental equations, Eqs. 11, 12. Assuming flow conservation in the network, a flow balance equation g_i is performed at each vertex v_i.

$$g_i = \sum_{v_k \in N(v_i)} q_{ij} - b_i = 0 \tag{11}$$

In this context, $N(v_i)$ represents the collection of neighboring vertices connected to v_i, and b_i signifies a parameter specifying the sources and sinks of the network, i.e. the vertices through which flow enters or leaves the network. Therefore, q_{ij} represents the flow in each of the blood vessels, connected by vertices i and j.

Aditionally, the linear system is derived by approximating the flow in each edge using Hagen-Poiseuille's law:

$$q_{ij} = T_{ij}(p_i - p_j) \tag{12}$$

Where T_{ij} represents the transmissibility of each edge and p_i and p_j the pressure in the vertices connected by the correspondent edge. The transmissibility is equivalent to the inverse of the effective flow resistance per each pipe.

$$T_{ij} = \frac{1}{R_{ij}} \tag{13}$$

Following R_{ij} the definition:

$$R_{ij} = \frac{128 l_{ij} \mu_{ij}}{\pi d_{ij}^4} \tag{14}$$

Adding this definition to Eq. 12 the resulting equation follows:

$$q_{ij} = \frac{\pi d_{ij}^4}{128 l_{ij} \mu_{ij}}(p_i - p_j) \tag{15}$$

Here, p_i and p_j represent pressures at two adjacent vertices v_i and v_j, while d_{ij}, l_{ij}, and μ_{ij} denote the diameter, length, and viscosity associated with pipe e_{ij}, respectively.

By merging Eqs. 11, 12, it becomes possible to compute the pressures and flow rates across the entire network, relying on the prevailing distribution of T_{ij}.

However, in this way, we are not taking into account the Fåhræus-Linquist effect. As mentioned in the introductory section, this effect is produced by the existence of the cell-free

layer and red blood cells. This effect notably changes the transmissibility of blood vessels, so it is necessary to add the effect of the relative apparent viscosity $\mu_{rel,ij}$ as established in Eq. 10. Adding this, the Eq.15 now looks as follows:

$$q_{ij} = \frac{\pi d_{ij}^4}{128 l_{ij} \mu_{ij} \mu_{rel,ij}} (p_i - p_j) \tag{16}$$

This relative apparent viscosity is calculated by the experimental equations formulated by Pries et al [14] and depends on the tube haematocrit and the vessel diameter.

$$\mu_{rel,ij} = \mu_{rel,ij}(H_t, d) \tag{17}$$

2.3.3 Treatment of red blood cells

In this study, the RBC presence is introduced by assuming a constant tube haematocrit of 0.3. Consequently, there is no individual tracking of red blood cells, and no specific rules or probabilities are applied to determine the direction of a red blood cell at a bifurcation. Since there is no tracking of these particles, such considerations would be irrelevant.

As explained in Section 2.2.2, the red blood cells do not have the same velocity as the mean plasma velocity due to the Fåhræus effect, i.e.,

$$u_{rbc,ij} = \frac{q_{ij}}{d_{ij}^2 \frac{\pi}{4}} \frac{H_{d,ij}}{H_{t,ij}} \tag{18}$$

where $H_{d,ij}$ represents the discharged haematocrit. The relation presented by Pries et al. [14] is used in this study to calculate the ratio $\frac{H_{d,ij}}{H_{t,ij}}$ following Eq. 19, based on the vessel diameter [m]:

$$\frac{H_{t,ij}}{H_{d,ij}} = H_{d,ij} + (1 - H_{d,ij}) \cdot (1 + 1.7e^{-0.35 D_{ij}} - 0.6e^{-0.01 D_{ij}}) \tag{19}$$

Fitting equations based on experimental data were developed for cases where H_t is known but H_d is not. In this project, it is assumed that $H_t = 0.3$, yet considering the Fåhræus effect and its dependence on diameter and haematocrit is essential.

$$H_{d,ij} = -\frac{X}{2 - 2X} + [(\frac{X}{2 - 2X})^2 + \frac{H_t}{1 - X}]^{0.5} \tag{20}$$

Here, the variable X represents the dependence on the diameter.

$$X = 1 + 1.7e^{-0.35D} - 0.6e^{-0.01D} \tag{21}$$

Furthermore, to calculate the relative apparent viscosity, the equations developed in the same work are also used to account for the Fåhræus-Linquist effect. Thus, these equations take the form:

$$\mu_{rel,ij} = 1 + \frac{\mu_{rel,ij,0.45} - 1}{(1 - 0.45)_{ij}^{C} - 1} \cdot [(1 - H_t)^{C_{ij}} - 1] \tag{22}$$

Being $\mu_{rel,ij,0.45}$ the relative apparent viscosity when having $H_t = 0.45$, as shown in Eq. 24.

$$C_{ij} = \left(0.8 + e^{-0.075 D_{ij}}\right) \left(-1 + \frac{1}{1 + 10^{-11} D_{ij}^{12}}\right) + \frac{1}{1 + 10^{-11} D_{ij}^{12}} \tag{23}$$

$$\mu_{rel,ij,0.45} = 220 \cdot e^{-1.3 D_{ij}} + 3.2 - 2.44 \cdot e^{-0.06 D^{0.645}} \tag{24}$$

Consequently, the relative apparent viscosity is calculated for every vessel of the network, since it depends on the diameter, affecting differently to the transmissibility of every vessel.

2.4 Optimization methods

Optimization methods are used for finding the best possible solution from a set of different choices. Usually, the algorithm aims to maximize or minimize the objective function or cost function.

Solving the forward problem yields the flow rate and RBC velocity of each vessel, as well as the pressures at the nodes connecting the different vessels. However, this does not provide the experimentally measured conditions. To achieve that, the resolution of an inverse problem is required.

In this study, the gradient descent algorithm is used, which is a local search algorithm for finding a minimum in the cost function [11]. More specifically, the Adjoint Method is employed because it is computationally less expensive.

In this section, the inverse problem is explained, for which the Adjoint Method is used.

2.4.1 Inverse problem

In the forward problem, the boundary conditions are employed to determine a singular solution for the distributions of flow and pressure within microvascular networks, contingent on a specified transmissibility field. Subsequently, the ensuing section introduces the inverse problem, elucidating the methodology to estimate the necessary adjustments to pressure boundary conditions P_l for inducing localized alterations in red blood cell velocities.

The variable α_l is introduced and initialized with the value of the boundary conditions and defined as follows:

$$\alpha_l = P_l \tag{25}$$

Here, l represents the index of the boundary condition. Note, that the presented algorithm is specifically for tuning pressure boundary conditions and equations would change if flow boundary conditions would be our target. In this way, the RBC velocity in a specific target edge e_t, is increased or decreased from a baseline state $u_{rbc_t}^{\text{base}}$ to a desired value $u_{rbc_t}^{\text{target}}$. The inverse problem is tackled through iterative solutions aimed at determining the optimal parameters that minimize a cost function J. This function encapsulates the objective of the inverse model, expressed as:

$$J(\nu) = \sum \left(\frac{u_{rbc_t}^{\nu} - u_{rbct}^{\text{target}}}{\sigma} \right)^2 \tag{26}$$

In this context, $u_{rbc_t}^{\nu}$ represents the velocity resulting from the current parameters $\alpha_l^{(\nu)}$ in iteration ν, and $J^{(\nu)}$ represents the corresponding value of the cost function. σ is used on order to normalize the differences, and the value of u_{rbct}^{target} is used for this purpose.

Another cost function is going to be used later, so in order to differentiate them, this cost function will be referred to as 'measurements' cost function.

The inverse problem is considered fully converged if u_{rbc}^{target} fits exactly. However, this is unlikely to happen in practice. Instead, the convergence criteria will be discussed during the presentation of the results.

Gradient descent can be used for finding the minimum of Eq. 26, adjusting the parameters proportionally to the gradient $\frac{dJ^{(\nu)}}{d\alpha_l^{\nu}}$, that is:

$$\alpha_l^{\nu+1} = \alpha_l^{\nu} - \gamma \frac{dJ^{(\nu)}}{d\alpha_l^{(\nu)}} \tag{27}$$

where γ is the learning rate. This problem is addressed using the Adjoint method, which is faster than conventional methods. With this approach, to calculate the gradient, it is only necessary to solve the forward problem once.

$$\frac{dJ}{d\alpha_l} = \lambda_i \frac{\partial g_i}{\partial \alpha_l} + \frac{\partial J}{\partial \alpha_l} \tag{28}$$

where the adjoint variable λ_i is computed with the adjoint Eq. 29.

$$\frac{\partial g_i}{\partial P} \lambda_i = -\frac{\partial J}{\partial P} \tag{29}$$

Using this method, Eqs. 11, 12 are solved at every iteration step, calculating the pressure field and the flow rates throughout the entire network. Once this is done, α_l is updated using Eqs. 27, 28, 29, leading to a reduced cost function value. This process is repeated until a predefined threshold is reached.

To effectively illustrate the problem and gain a deeper understanding, we will explain the development of this gradient and its various components. First, we calculate the vector λ. For this purpose, we need to determine $\frac{\partial g_i}{\partial P_l}$ and $\frac{\partial J}{\partial P}$. Starting with the former, we follow Eq. 11, and from the definition of flow, Eq. 12, we obtain the same transmissibility matrix used in solving the direct problem. Thus, it is a square matrix with a size equal to the number of vertices in the network.

On the other hand, to calculate $\frac{\partial J}{\partial p}$, the chain rule must be applied. The variable dependent on pressure in the definition of the cost function is $u^{\nu}_{rbc_t}$. Therefore, this partial derivative is given by:

$$\frac{\partial J}{\partial P} = \frac{2(u^{\nu}_{rbc_t} - u^{\text{target}}_{rbc}t)}{\sigma} \cdot \frac{Tij}{d^2_{ij}\frac{\pi}{4}} \frac{H_{d,ij}}{H_{t,ij}} \tag{30}$$

In this case, it is a matrix with dimensions [number of target velocities $\times$ number of vertices]. Once we have these two partial derivatives, we can proceed to calculate the vector λ.

Once we have obtained λ, the only remaining task is to determine $\frac{\partial J}{\partial \alpha_l}$ and $\frac{\partial g_i}{\partial \alpha_l}$. If we examine the first of them, and the definition of the cost function and α_l, we realize that this derivative is 0 assuming there are no target velocities given to a boundary edge. This is because the target velocities are associated with blood vessels, while α_l is defined at boundary conditions, which are vertices. In the case where there are target veocities in the bundary edges, this term will be non-zero and take the form of Eq. 30, as the boundary node pressure appears in the cost function J.

Finally, $\frac{\partial g_i}{\partial \alpha_l}$ is a matrix of dimensions [number of vertices $\times$ number of α_l parameters]. Following the definitions of α_l and g, its derivative is -1 where the pressure corresponds to one of these vertices with the α_l parameter.

All the aforementioned details are crucial for defining the problem and serve as the starting point for the studies conducted in this project. However, adjustments will be made, as explained later, justified by the results obtained.

2.5 State of art

With the objective of summarizing the studies from which this work originates and relevant research in the field of microstrokes and blood vessel simulations, we begin with the thesis by Robert Epp, titled "Inverse Model for Biphasic Blood Flow in the Microcirculation: Predicting Structural and Functional Characteristics of Microvascular Networks." This work addresses the complex vasodynamics of the brain's blood supply, especially during neuronal activity and ischemic stroke. Utilizing numerical simulations, the study develops an inverse model to infer vascular parameters like vessel diameters based on flow characteristics. This inverse model is the one used for the present study.

Furthermore, Schmid et al. [16] delve into the depth-dependent flow and pressure characteristics within cortical microvascular networks, offering insights into the complexities of

blood flow at various depths of the cortex, which is pertinent to understanding microstroke dynamics and the localized effects of blockages in cerebral circulation.

Additionally, in another study, Schmid et al. [18] examined the impact of vasodilation on blood flow and RBC distribution within microvascular networks. This research illuminates how capillary dilation influences the microvascular hemodynamics.

Moreover, Epp's work on inverse problems in blood flow simulations tackles the methodological challenges in predicting and managing the changes in vascular diameters [7]. The same inverse problem is utilized in this study for the tuning of boundary conditions, but with a change in the definition of the variable alpha and all its consequences, since it is the pressures that are tuned, not the diameters.

Significantly, Schmid et al. [17] study contributes to the understanding of blood flow stabilization in microvascular networks by RBCs, highlighting the importance of cellular components in maintaining flow stability.

Lastly, the study on bifurcation types in microvascular networks [19] addresses the structural variations and their implications for blood flow patterns, essential for modeling and predicting the outcomes of microstrokes where such bifurcations play significant roles in flow redistribution following vascular blockages.

In contrast to previous studies that focus more on changes in vessel diameters, this work aims to contribute insights into the pressures at the boundaries of the capillary bed. Assuming that the diameters of the network are well-approximated, this study emphasizes tuning the boundary pressures. This approach is distinct from others, like the work of Robert Epp and Schmid et al., where the primary focus is on varying diameters to understand microvascular dynamics and flow redistribution. By concentrating on boundary pressures, this research seeks to provide a deeper understanding of the hemodynamic responses in capillary networks during microstrokes.

3. Methodology

During this section, all steps taken to execute the study are described. Before the final study, a preliminary study was conducted to select the method that will be used to induce microstroke in the final study, among other things that will be explained in section 6. This section describes the methodology for both studies.

Generally, there are three important and distinct processes in the methodology of both studies.

- Pre-processing: the entire process of preparing the network for accurate interpretation in the simulation, as well as the CSV files containing data from experimental measurements, which are used as target values. Additionally, it includes the preparation for running all the simulations consecutively for the preliminary study, having randomly selected the target velocities, the capillaries where occlusion occurs, etc.
- Running the simulations
- Post-processing: once the simulations are completed, the next step involves the visualization and analysis of the outputs obtained. Calculations of various concepts and variables are also performed to aid in interpreting the results and to better understand the simulations.

Both the pre-processing and post-processing are carried out using Python, Paraview, and Excel.

3.1 Preliminary study

Before using the actual capillary network, a subset was extracted from a larger network. This subset includes the velocities of red blood cells in all blood vessels. Consequently, a random selection of 15 of these velocities was made for use as target values in solving the inverse problem. Note that none of the velocity constraints was directly at the boundary and consequently $\frac{\partial J}{\partial \alpha_l}$ is equal to 0. Otherwise, the problem is adressed in a similar manner to how it will be handled with the final capillary network for this study.

The primary objective of the preliminary study is to gain a clear understanding of the method to assign pressure boundary conditions yielding realistic flow fields both during baseline and during the microstroke. Two envisaged approaches for simulating the microstroke are as follows:

- Microstroke setup 1) Tuning boundary conditions before and after decreasing the diameter of the occluded capillary (microstroke). The stroke case is initialized with the solution of the baseline case.
- Microstroke setup 2) Tuning boundary conditions only before microstroke (i.e., baseline) and then solving the forward problem under microstroke conditions (i.e.,decreasing the diameter of the capillary occluded) using the baseline boundary conditions.

Within the first option of simulating the microstroke, it is crucial to analyze how the the resulting pressure boundary conditions and the resulting flow field change based on the location of the blockage within the network. Specifically, whether it is in proximity or distant from the boundary conditions. This analysis is logical as the proximity to a boundary condition will likely lead to more significant variations. A change in pressure at such a boundary condition will have a more direct impact on the velocity or flow rate of the blocked capillary. Ideally, to facilitate a meaningful comparison between simulations with and without microstroke, achieving an identical or closely similar solution is optimal. This entails obtaining a similar pressure value at the boundary conditions to ensure that any changes in the network's flow are solely attributed to the effects of capillary blockage.

The comparison of results obtained from simulating the blockage through two distinct methods will encompass an exploration of the influence exerted by the initialization of boundary conditions and the topology in the vicinity of the blockage.

This analysis aims to clarify how the simulation method, boundary condition initialization, and local topology interrelate, crucial for assessing the simulation's reliability and robustness.

In Figure 8, the steps taken in the preliminary study are generally described.

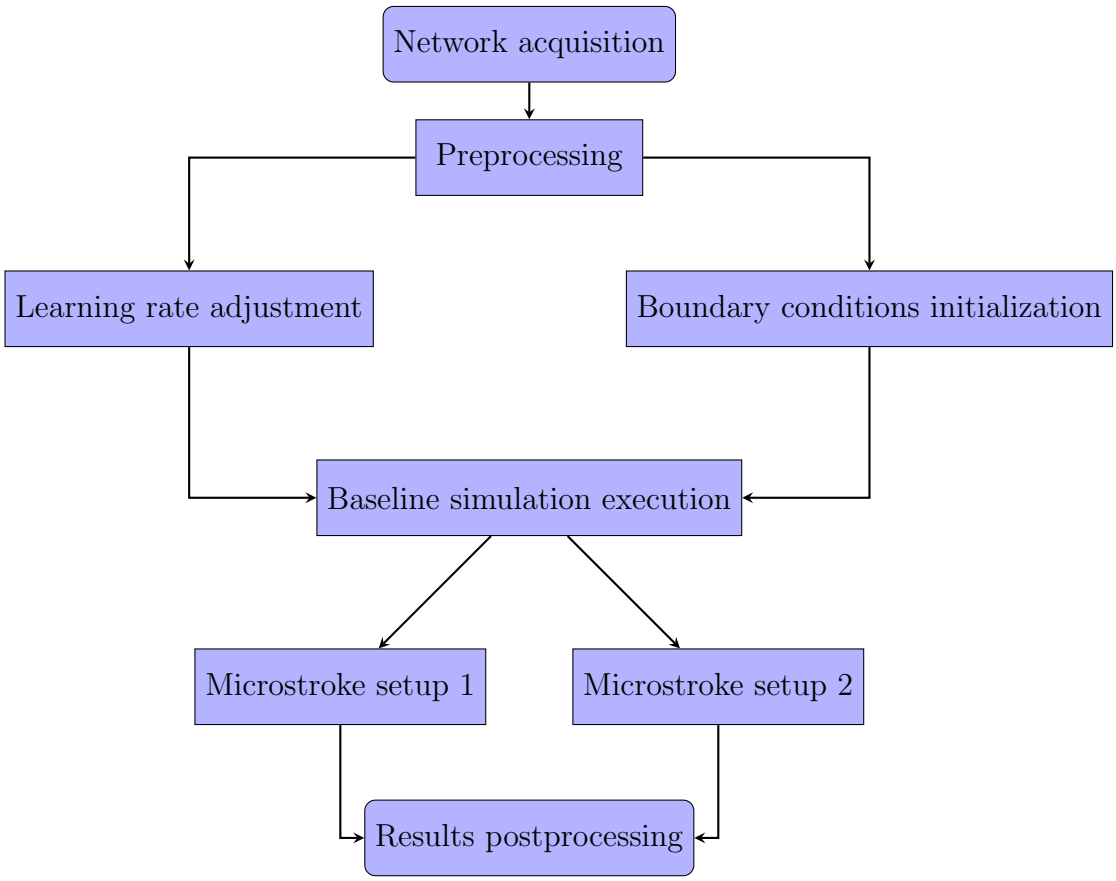

Figure 8: Preliminary study flowchart

After visualizing and analyzing the results, conclusions are drawn regarding which method

will be used in the final study to induce the blockage.

3.2 Final study

Once the capillary network, where some red blood cell velocities have been measured, is established, the final and main objective of the study is then pursued.

In the final study, the goal was to reach the experimentally measured velocities in certain capillaries while obtaining a physiologically realistic solution for healthy and microstroke conditions. This included differentiating between arteries and veins in the network to initialize the pressure of the boundaries.

A critical aspect of the methodology was the exclusion of certain measurements due to significant mass balance errors. This ensured the accuracy and reliability of the simulation results.

Both the baseline and microstroke simulation were conducted. First the baseline simulation is carried out and later the pressure solution is taken to initialize the microstroke simulation. This involved analyzing the flow and pressure changes within the network to understand the physiological impacts of microstrokes.

Key concepts such as capillary occlusion, bifurcation types, and the influence of local topology on simulation results were thoroughly examined. The study used the concept of "generations" to categorize vessels in relation to the occlusion site, facilitating a detailed analysis of the network's response to induced microstrokes.

The primary objective of the study is to compare healthy conditions with those occurring during a microstroke. Therefore, the study concludes with this comparison, examining changes in direction, CBF, and overall alterations in the flow.

The main steps taken to conduct the final study can be seen in Figure 9.

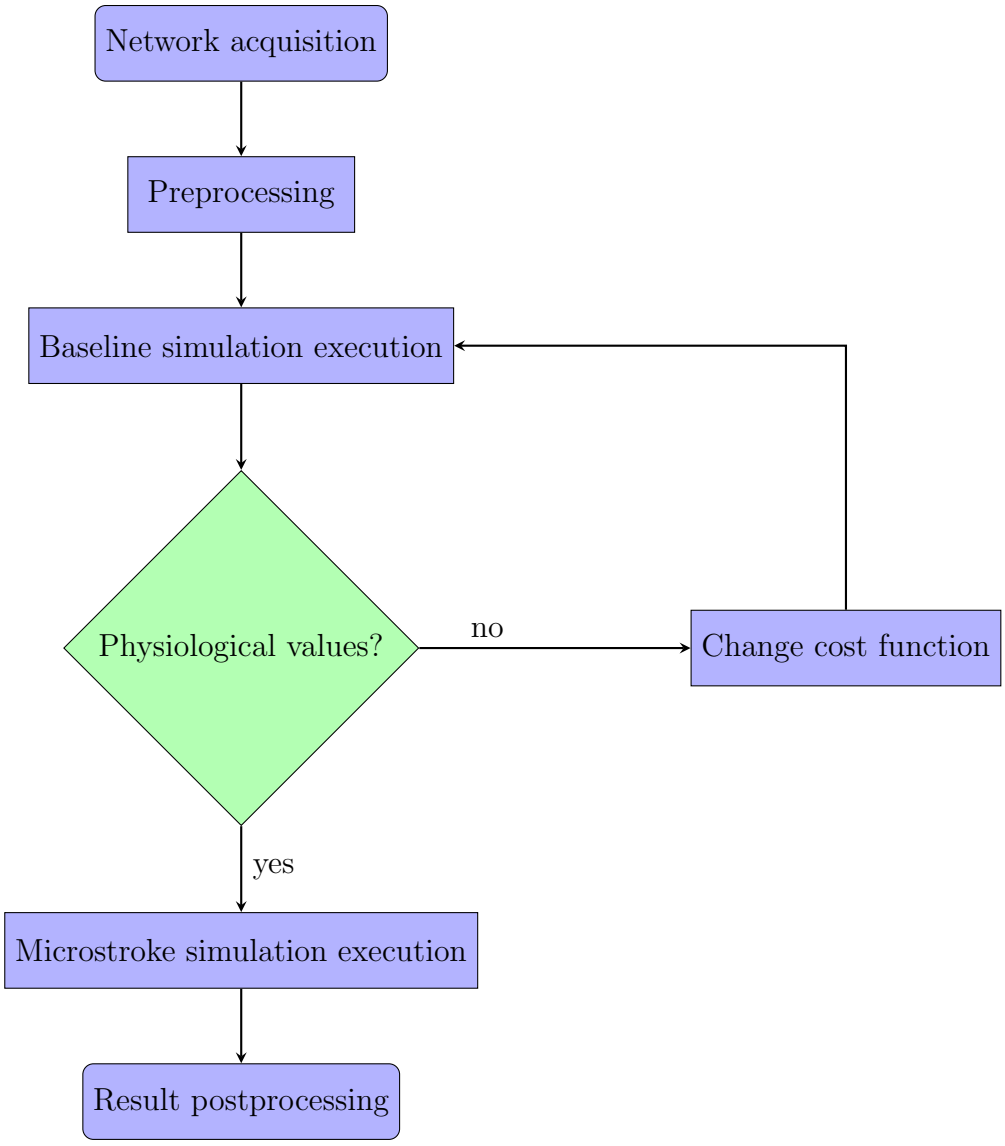

Figure 9: Final study flowchart

In post-processing, the graphs are obtained to make the comparison between healthy conditions and blockage conditions.

4. Detailed research process

In this section, each of the processes completed to conduct the study is described in detail, including all intermediate and preliminary steps leading to the final study.

4.1 Creation and source of the capillary networks

The vascular network utilized in the preliminary study represents a subsection extracted from a larger network available from the work from Schmidt et al [16].

The visualization and analysis of the cortical vasculature network for the final study involved employing a two-photon laser scanning microscope to visualize cortical vasculature by intravenously injecting a fluorescent dye, specifically Texas Red dextran. Line scans along the vessel midline were performed to measure RBC velocity. This was done by collaborators at the Institute of pharmacology and toxicology at the University of Zurich (group of prof. Bruno Weber). The two-photon experiments were conducted using a custom-built microscope equipped with a Titanium-sapphire laser. Processing of line-scan data was performed using MATLAB. Microstroke induction involved injecting a microstroke-inducing probe via a tail vein catheter, followed by targeted irradiation of capillaries.

To segment the 3D volumes, the volumes were sliced into 2D slices, and the Li algorithm (an algorithm for binarization of gray-level images) was applied to determine the threshold. Subsequently, noise removal and surface smoothing techniques were applied, and the segmentation was exported to 3D Slicer for centerline extraction.

This comprehensive process integrated various imaging techniques, segmentation algorithms, and experimental procedures to effectively visualize and analyze RBC velocities in the cortical vasculature.

4.2 Preliminary study

In this section, a detailed explanation is provided, and some results obtained in intermediate steps of the study are presented.

4.2.1 Learning rate adjustment

Before delving into the examination of the repercussions of blocking a capillary on boundary condition pressures, blood flow rates, and red blood cell velocities, a pivotal step is the meticulous adjustment of the γ parameter. This parameter, called learning rate, holds a significant role in the optimization process, as expounded in Section 2.4.1. The critical analysis of the optimal γ value is imperative, given its profound impact on the simulation outcome. It is noteworthy that a higher γ value enhances simulation speed; nevertheless, an excessively elevated value might instigate oscillation issues or even render the discovery of a feasible solution infeasible. Throughout this investigation, various values of the parameter were subject to consideration. However, the ensuing results are exclusively presented for three distinctive values, offering a focused and insightful exploration of the parameter's influence.

To assess the extent and significance of the variations in the solution resulting from different γ values under identical conditions, we scrutinize the relative changes in boundary condition pressures and blood flow rates across all vessels in the network. This comparative analysis provides insights into the impact of gamma on solution stability and sheds light on the sensitivity of the model to variations in this crucial parameter. This relative change is defined by:

$$rel_{change} = \frac{|q_{\gamma=500} - q_{\gamma=10}|}{|q_{\gamma=10|}} \tag{31}$$

The same formula applies for the pressure relative change in the boundary conditions. As depicted in Figure 10, both pressure and blood flow rate changes are negligible. This means that increasing the learning rate value does not significantly change the obtained solution, allowing for a higher value to be used, thereby speeding up the simulations. Therefore, the highest value (200) is chosen for conducting simulations, striking a balance between computational efficiency and solution stability. Opting for a higher value was avoided due to observed issues, such as oscillations and stabilization challenges, especially in cases involving capillary occlusion. This careful selection ensures an optimal balance, minimizing computational time without compromising solution reliability.

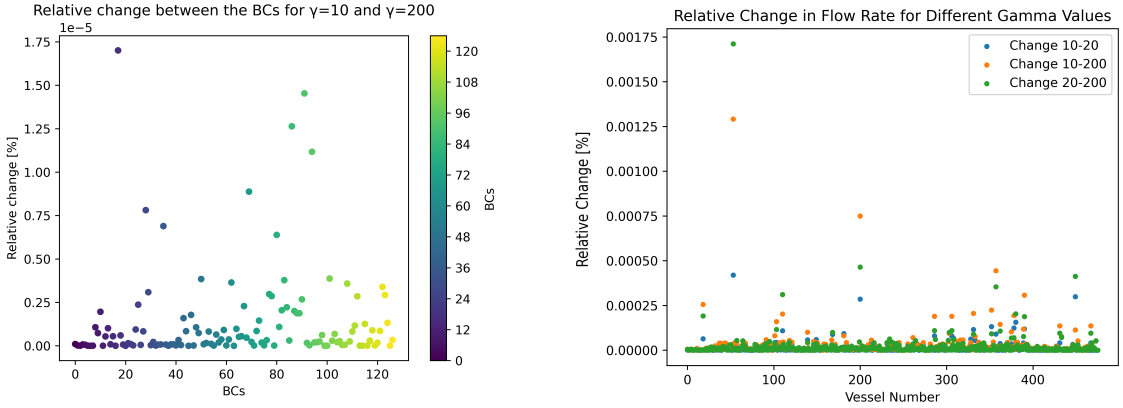

(a) (b)

Figure 10: (a) Boundary condition pressure relative change (b) Flow rate relative change.

4.2.2 Boundary condition initialization influence

The initialization of boundary conditions assumes a pivotal role in shaping the solution, as different starting points can lead to divergent outcomes. Assessing the impact of this initialization ensures a comprehensive understanding of the sensitivity of the simulation results to the chosen conditions.

Different initializations can lead the system to converge to different solutions, depending on proximity to local minima. To address this, a comparison is made between two distinct initialization scenarios. The first involves assigning random values (ranging from 15 to 45

mmHg) to each boundary condition, reflective of typical capillary network pressures. The second approach sets a uniform initial pressure of 20 mmHg for all boundary conditions. This comparative analysis provides insights into how different initializations impact the solution space and convergence behavior.

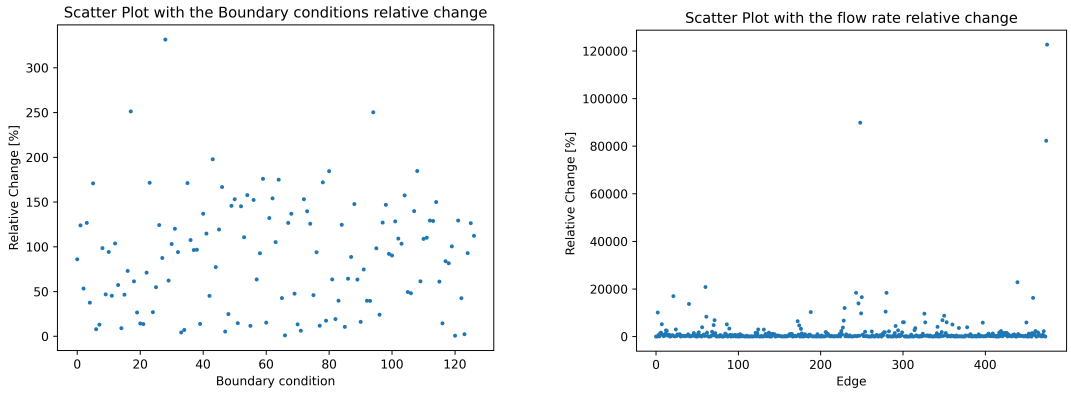

(a) (b)

Figure 11: (a) Boundary condition pressure relative change (b) Flow rate relative change when initializing differently the boundary condition's perssure.

As depicted in Figure 11, a substantial shift in pressure values is evident at the solution of the two simulations. This disparity in pressures significantly impacts the flow field, leading to a complete alteration in the blood flow rates within the network vessels. The resulting solutions are entirely distinct and bear no resemblance to each other. As observed, pressure changes can reach up to 300% in some cases, which in turn causes even larger changes in flow, with several thousand percent change in flow rate. These data are also represented in boxplots in Figure 12, where it can be seen that the average change in flow is around 1800%.

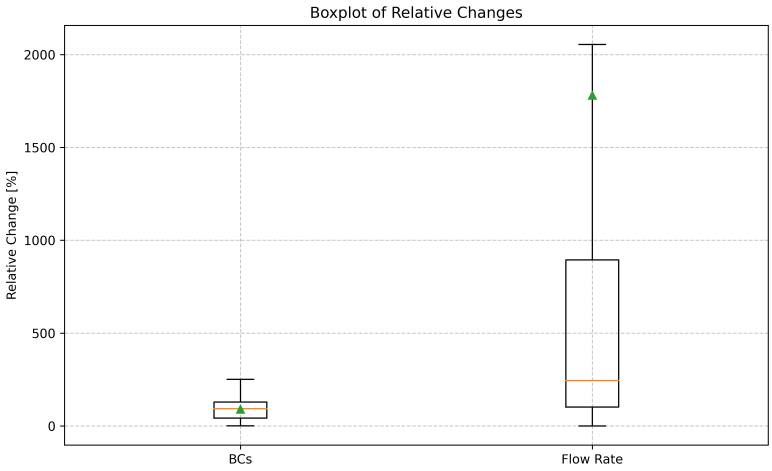

Figure 12: Boxplot with the pressure and flow rate relative change values. Orange lines represent the median and the green triangles the mean.

Hence, the initialization of boundary conditions plays a crucial role in determining the simulation outcome. Therefore, special attention must be paid to this aspect in future endeavors to converge towards the desired solution.

4.2.3 Microstroke setup 1 - Methodology and convergence criteria

The steps undertaken for this purpose are as follows:

1. A simulation is executed by selecting 15 random targets with no blocked edges. This simulation will serve as the baseline.
2. 20 individual edges are chosen randomly to be blocked, ensuring coverage across all sections of the network, including the border and center.
3. Each of these blocked edges is individually added to the 15 targets as a 0 velocity constraint.
4. 20 simulations are conducted, each with a different location for the blocked edge.
5. The results of these 20 simulations are then compared with the baseline simulation.

Regarding the convergence criteria, the simulation stops when all these objective values are achieved with an error of 1% above or below the target, and when the cost function has decreased by at least 3-4 orders of magnitude compared to its initial value. Additionally, the boundary condition pressures should not change significantly throughout the iterations, indicating a stable value has been obtained for all of them. The same is applied for the target velocity values.

Figures 13 and 14 provide a visual representation demonstrating the fulfillment of the specified conditions.

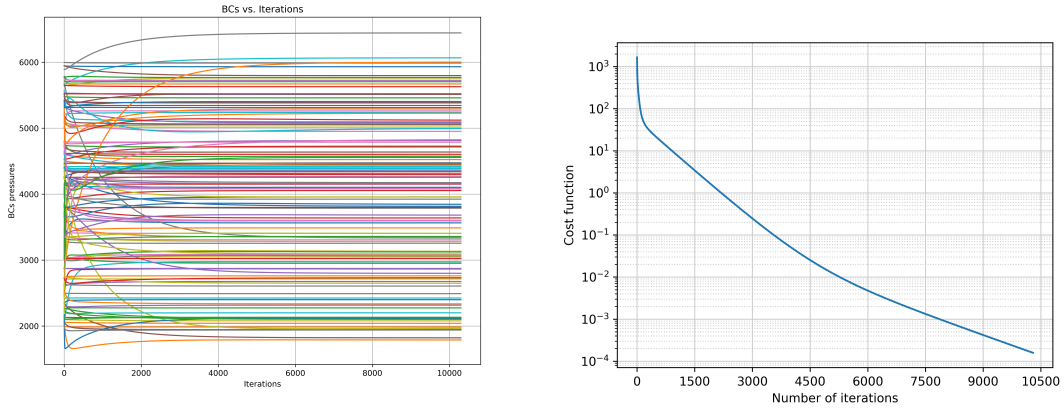

(a) (b)

Figure 13: (a) Boundary conditions throughout the iterations (b) Cost function value throughout the iterations.

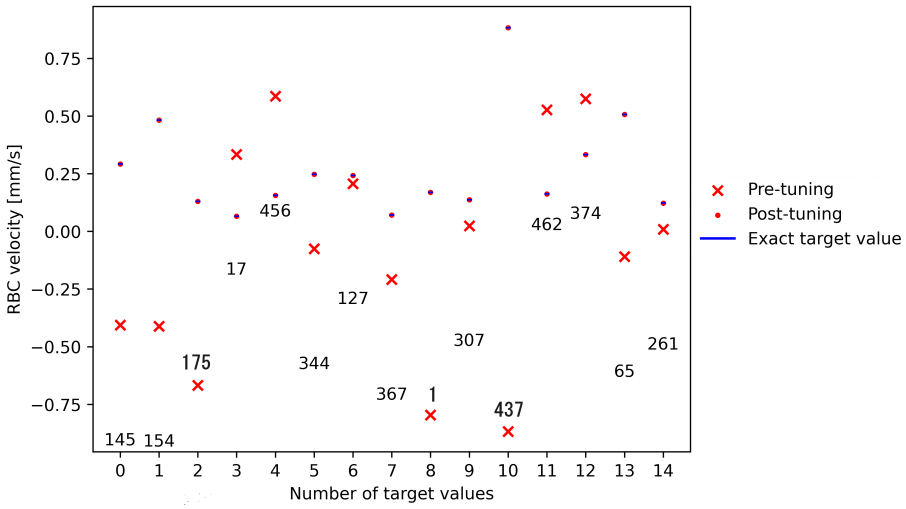

Figure 14: Target values along with their final achieved values.

As depicted in the figures, all convergence criteria are satisfied. It can be observed that the pressure value at the boundaries reaches a flat level that stops changing with the progress of iterations, while the cost function value drops significantly compared to its initial value at the start of the simulation. Additionally, all target values are met, thus ensuring the convergence of the simulation.

4.2.4 Microstroke setup 2 - Methodology

The steps carried out to solve the forward problems are as follows:

1. A simulation is run selecting 15 random targets with no blocked edges. This is used as the baseline (same as in Section 4.2.1).

2. 20 random edges are selected to be blocked edges, one per simulation.
3. The diameter of each of these edges is decreased by 99%.
4. 20 simulations are run, each with a different location of the blocked edge, solving the forward problem.
5. These 20 simulations are compared with the baseline simulation.

4.2.5 Key Concepts in Capillary Occlusion

This study aims to explore stroke induction by applying 15 predetermined velocities within the network to observe if pressures near the boundary conditions exhibit more pronounced changes compared to those at greater distances. The focus is also on examining the flow alterations proximate to the stroke, including directional changes. The examination of the topology in the proximity of the blockage becomes imperative. The intricate interplay between vessel arrangement and the specific location of the blockage can significantly mold the simulated outcomes. Variations in the topology may introduce nuanced changes in flow dynamics, necessitating a meticulous analysis to discern the extent of these influences on the overall solution.

The term "generations" is used to denote the blood vessels surrounding the occlusion. The occluded vessel is considered Generation 0, vessels connected to it form Generation 1, those connected to Generation 1 vessels form Generation 2, and so forth. This relationship can be observed in an example of occlusion presented in Figure 15.

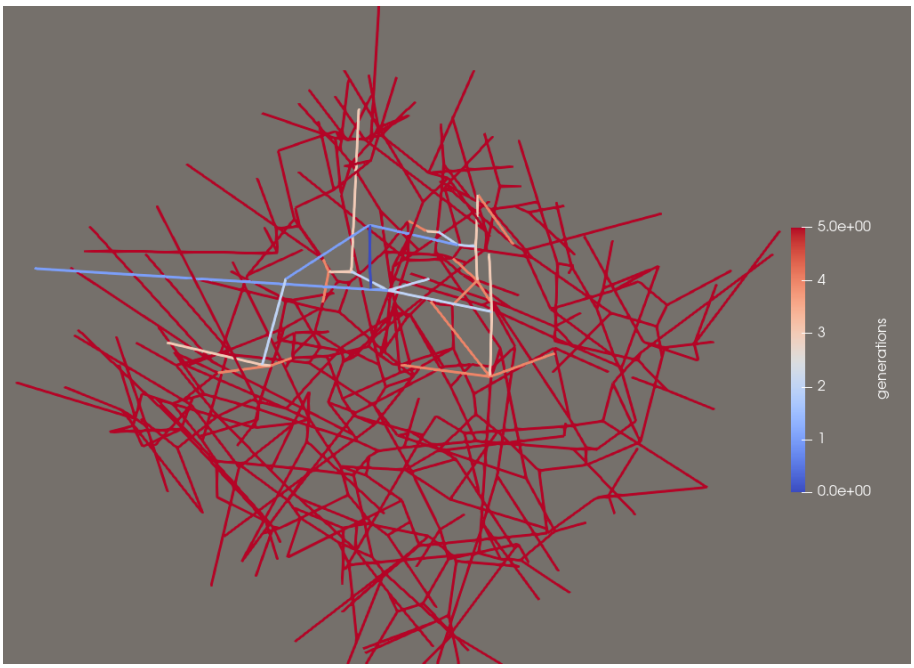

Figure 15: Example of the generations used for one blocked edges chosen (dark blue).

Additionally, the study intends to assess the impact of local topology at the occlusion site. Specifically, it will investigate how the changes vary with different types of bifurcations where

the occlusion takes place, defining the bifurcation types based on the count of inflows and outflows at the blocked capillary, as described by Schmid et al [16]

In microvascular networks, bifurcations are critical points where a single blood vessel splits into two or more branches. These bifurcations can be classified based on their topological structure, primarily by the number of flow inlets before occlusion occurs. There are four main types:

1-in-1-out: In this type, one blood vessel (the block one) divides into two, one being an outflow and the other one an inflow. It represents a basic branching pattern where one inlet vessel bifurcates into two outlet vessels.

2-in-1-out: In this configuration, two inlet vessels converge into a single outlet vessel. It reflects a merging pattern where two incoming vessels join to form one outgoing vessel.

1-in-2-out: This type involves a single inlet vessel splitting into two outlet vessels. It signifies a diverging pattern where one incoming vessel divides into two outgoing vessels.

2-in-2-out: Here, two inlet vessels split into two outlet vessels each. It represents a complex pattern where two incoming vessels bifurcate, resulting in four outgoing vessels.

These bifurcation types play a crucial role in determining flow distribution and hemodynamic characteristics within microvascular networks. However, not all types of bifurcations are equally common. The 2-in-2-out bifurcation is the least frequent, accounting for approximately 8% of occurrences, as highlighted in [19].

These four types can be observed in Figure 16.

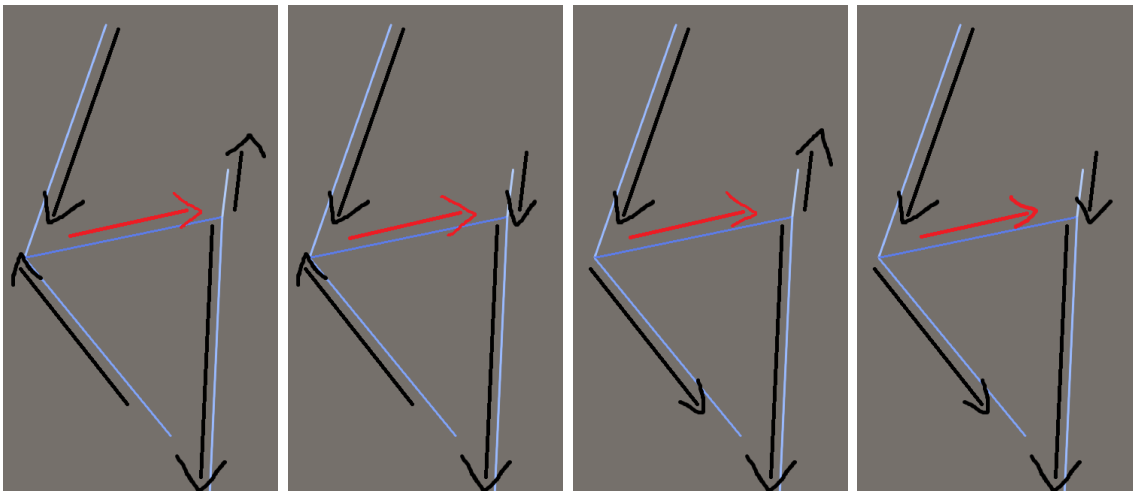

(a) (b) (c) (d)

Figure 16: (a) 2-in-2-out (b) 2-in-1-out (c) 1-in-2-out and (d) 1-in-1-out.

4.3 Final study

4.3.1 Measurements, Arteries and veins identification

As explained earlier, we have various experimental measurements of red blood cell velocity in different capillaries of the network. These measurements were annotated in the segmentation manually, indicating the direction and assigning different numbers for their distinction. The same procedure was applied to the stack images obtained from vascular imaging. Additionally, descending arteries and ascending veins that could be distinguished in the network were also marked in these images. Therefore, the first step to carry out the study is to assign the experimental measurements and arteries and veins in the network obtained from segmentation.

This identification was performed using ParaView along with the aforementioned stack images and segmentation. First, the network and segmentation were overlaid to identify which capillary corresponds to each measurement.

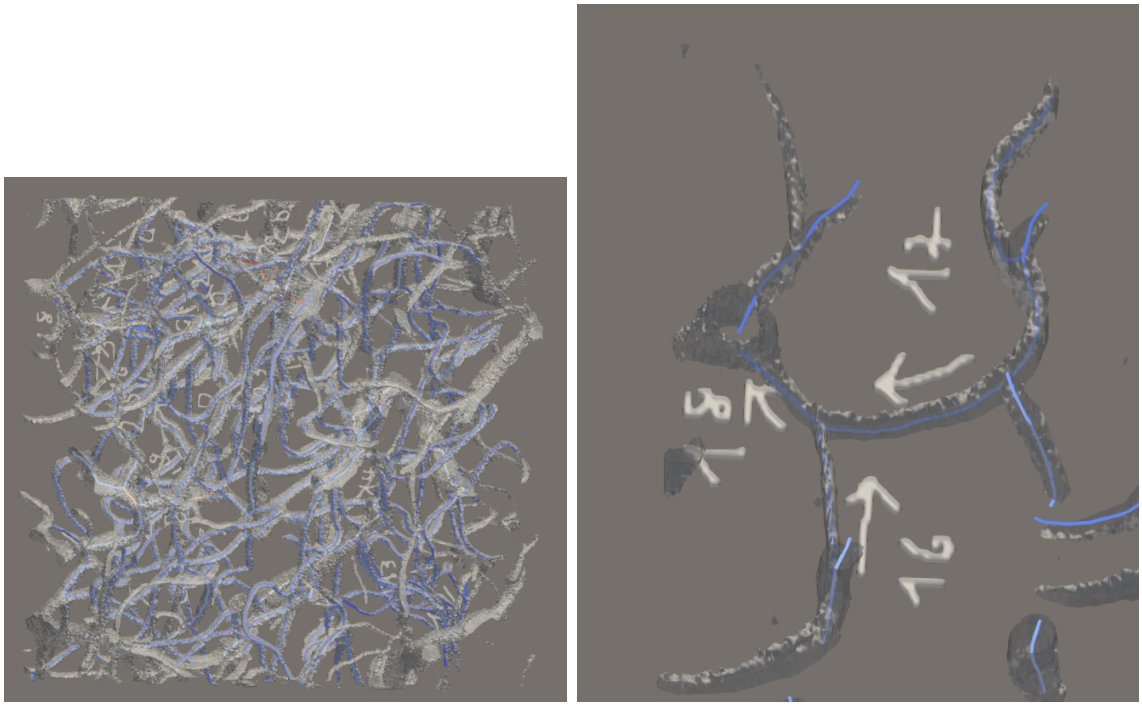

(a) (b)

Figure 17: (a) Segmentation and network vtp file superposed (b) Example of the manual indications of the measurements in the segmentation

Subsequently, this was double-checked with the stack images to confirm that all measurements were correctly identified, along with their direction.

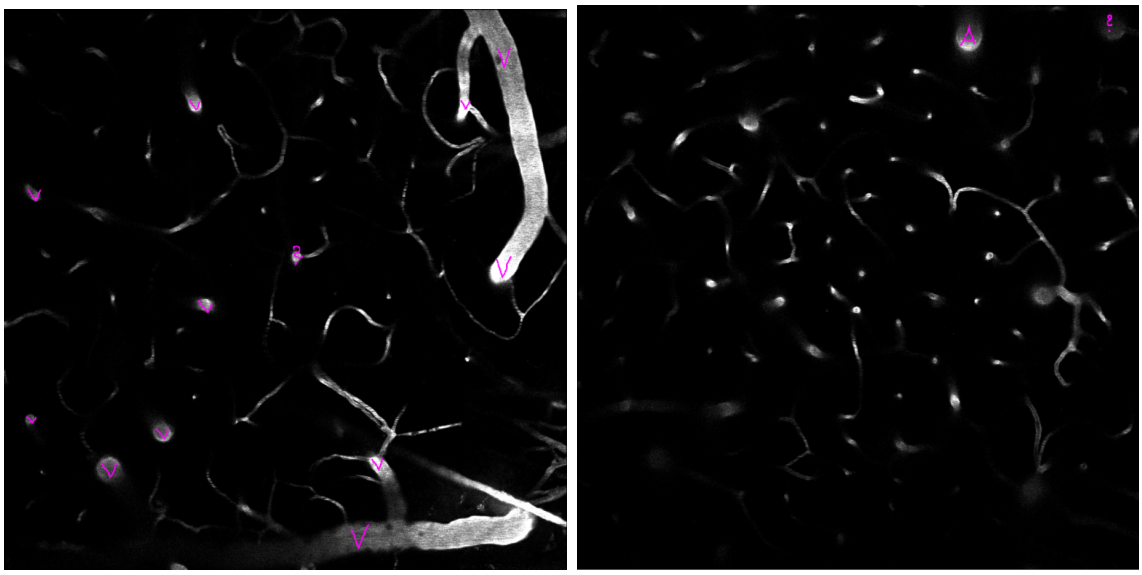

(a) (b)

Figure 18: (a) Veins indication in the stack images. The question marks correspond to blood vessels whose type (vein or artery) is not known. (b) Artery indication in the stack images

The outcome of the identification of veins and arteries can be seen in Figure 19.

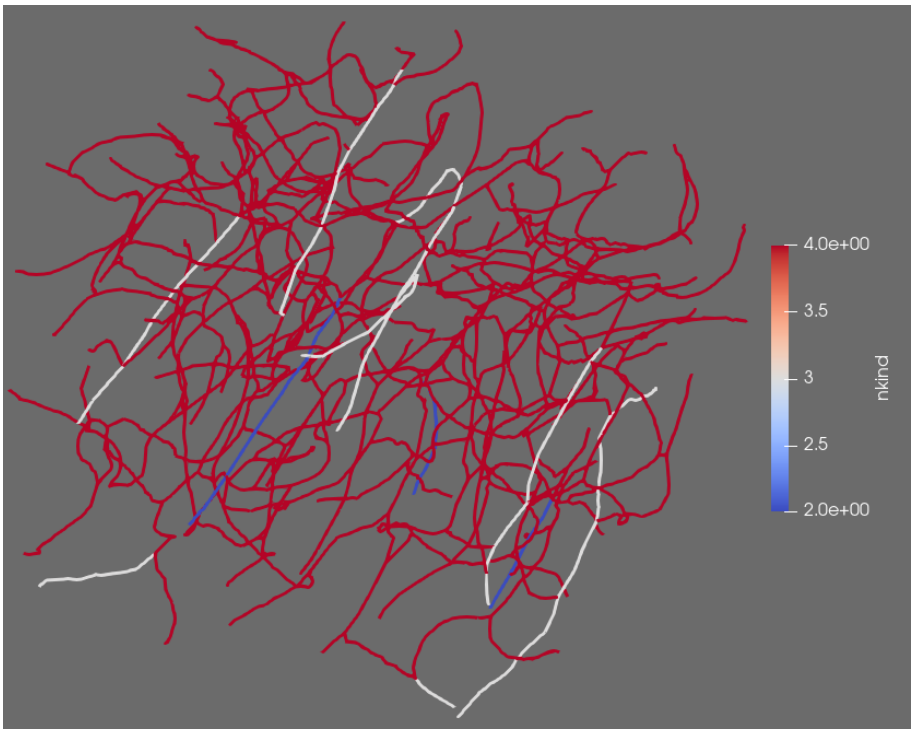

Figure 19: Visualization of the network in ParaView differentiating the vessel type. 2 refers to artery, 3 to vein and 4 to capillary.

Identifying veins and arteries was a slightly more complicated process as they could not

always be marked in the segmentation. First, the marked vein/arteries in the stack images were identified in the segmentation by scrolling through the different captures and following the vessel shape to identify it in the segmentation. Once identified, the same process as before was carried out to identify it in the VTP file.

Due to the segmentation being slightly larger than the network, some of the measurements located at the edges of the segmentation do not correspond to vessels in the network. As a result, although there were initially 27 experimental measurements, 3 of them were in this situation and could not be used.

For a better understanding of the network and the simulations conducted, in Figure 20, the boundary nodes are shown in pink. These nodes are where the pressure is adjusted to achieve the experimental velocities. The edges in green represent the capillaries in which these experimental measurements are taken, and the red represents the capillary where the stroke is subsequently induced.

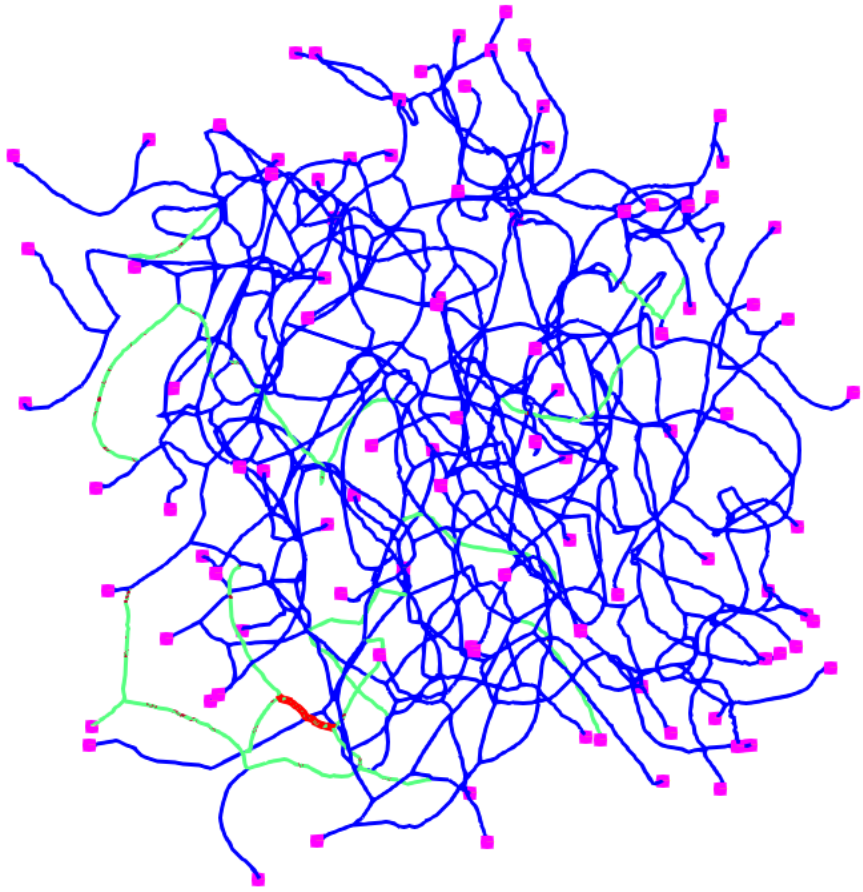

Figure 20: Network visualization in ParaView highlighting the boundary nodes (pink), experimental measurements (green) location and blocked capillary (red).

In Table 2, a summary of the characteristics of the network used for the final study is presented. It is noteworthy that two of the three arterial trees were not easily identifiable, raising the possibility that they may not be arteries in reality. In fact, in the initial baseline

simulations, two of these trees have very low pressures, which correspond to those that were difficult to identify. Therefore, for the simulations in the final study, only one of these three trees is considered.

Table 2: Summary of the network's characteristics

Number of capillaries	340
Number of veins	31
Number of arteries	8
Number of Boundary nodes	99
Number of measurements	24
Total number of vessels	379
Total number of nodes	310

4.4 Boundary conditions initialization

As seen in Section 4.2.2, initializing the inverse problem with values consistent with the desired outcome is crucial, as different initializations will lead to very different solutions.

Therefore, two large networks used before in a previous project [16] were utilized. These networks contain both pial veins and arteries, as well as the capillary bed, along with ascending veins and descending arteries. The arteries and veins in our network are DAs and AVs. Thus, these were identified in the two networks, and the mean, median, and standard deviation of their pressure values were calculated. These values are shown in the following table.

Table 3: Pressure values obtained for DAs and AVs

	Descending arteries	**Ascending veins**
Mean	47.9	10.9
Median	48.1	10.4
Standard deviation	8.4	1.0

Regarding the capillaries, the same procedure was followed, but they were divided into different groups depending on the depth in the network they were located. The mean, median, and standard deviation were also calculated for each depth range.

Table 4: Mean, median and standard deviation pressure for the capillaries in function of the depth

Mean Pressure [mmHg]	Median Pressure [mmHg]	Std Deviation [mmHg]	Depth [μm]
18.4	18.5	2.9	0 – 25
15.6	14.9	3.4	25 – 50
18.8	17.1	6.5	50 – 100
18.0	16.4	6.0	100 – 200
18.6	17.5	4.9	200 – 300
19.9	18.8	4.7	300 – 400
20.9	20.2	4.3	400 – 500
21.4	21.2	3.5	500 – 600
22.0	21.8	3.0	600 – 700
22.3	22.1	2.5	700 – 800

Thus, the median was chosen as the value to initialize arteries and veins. As for the capillaries, a random value between the median ± std/2 was chosen since there is more variation in their values. The two first ranges are smaller since in the proximity to the surface there might be more variation in the pressure values.

4.4.1 Excluded measurements

In the network, we have a total of 24 measurements of red blood cell velocities. However, some of them are in neighboring capillaries and are accumulated in a specific area of the network. This occurs around the capillary where the blockage was experimentally induced. Here, in 4 nodes, we would be assigning a value to each of the edges that leave those nodes. Therefore, considering that the experimental measurements have a certain error and are not recorded simultaneously, the mass balance error was calculated at these nodes. To do this, Eq. 18 was used to calculate the flow rate from the red blood cell velocity, and Eq. 11 for the mass balance. The formula used to calculate the mass balance error is now defined:

$$\text{Mass balance error } [\%] = \frac{(\text{Incoming flow} - \text{Outgoing flow})}{\text{Incoming flow}} \times 100 \tag{32}$$

Where:

- *Incoming flow* is the sum of all flow rates entering the node.
- *Outgoing flow* is the sum of all flow rates leaving the node.

For the mass balance calculation, the incoming flow is considered positive, while the outgoing flow is considered negative.

Table 5: Mass balance error in the nodes where we have a measurement in all of the edges. Balance represents the difference between incoming and outcoming flow. The error represents the mass balance error

Node 221				
Edge	**RBC velocity** $[\frac{m}{s}]$	**Flow rate** $[\frac{m^3}{s}]$	**Balance** $[\frac{m^3}{s}]$	**Error** [%]
268	-1.95E-03	-1.70E-14		
269	1.60E-03	1.10E-14	7.47E-15	30.5
228	1.03E-03	1.35E-14		
Node 124				
169	1.13E-03	8.15E-14		
122	-2.95E-03	-7.82E-14	8.22E-14	51.2
170	3.00E-03	7.88E-14		
Node 164				
170	-3.00E-03	-7.88E-14		
162	1.71E-03	1.42E-14	-2.84E-14	56.2
220	2.55E-03	3.63E-14		
Node 215				
220	-2.55E-03	-3.63E-14		
263	1.28E-03	1.26E-14	-4.83E-15	15.3
264	2.01E-03	1.88E-14		

It is observed from table 5 that there is a considerable error in the mass balance. Therefore, to ensure that mass balance can be achieved and all target values can be reached, different measurements were excluded. This exclusion process is illustrated in Figure 21.

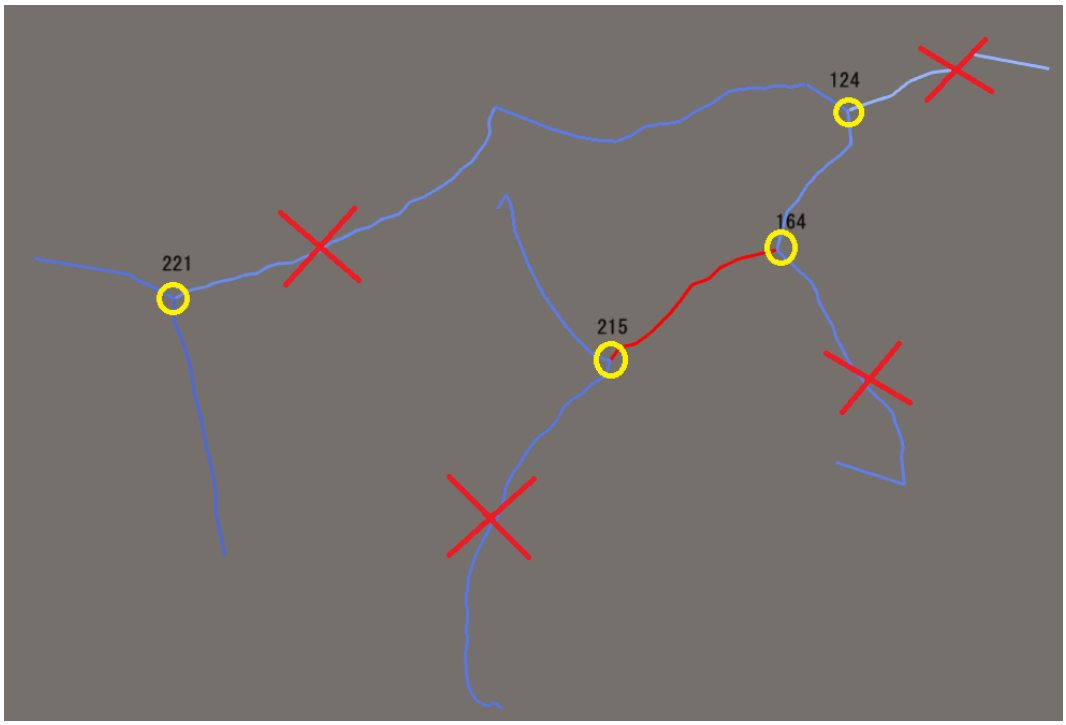

Figure 21: Excluded measurements around the edge is going to be blocked (red)

4.4.2 Generations

In the context of the final study, the definition of "generations" is adapted to consider the direction of flow when calculating these generations. Therefore, the terms "upstream" and "downstream" vessels are defined in relation to the occlusion, following the definition of [19].

"Upstream vessels" refer to those vessels that lead to the site of occlusion, essentially the paths through which blood flows towards the blockage. Conversely, "downstream vessels" are those that lead away from the occlusion site, representing the paths through which blood flows after passing the blockage point.

4.5 General key concepts

4.5.1 Distance calculation

In the preliminary study, an analysis is conducted to assess how much the pressure value changes at the boundary nodes in relation to the distance from the blockage. For this purpose, quartiles are used.

To achieve this, the Euclidean distance is used, which can be defined as the straight-line distance between two points in a multidimensional space. According to the Euclidean metric, this distance is calculated by taking the square root of the sum of the squared differences between the coordinates of the points [27]. Additionally, the number of edges from the occluded edge to each boundary node is also employed, as well as the sum of the lengths

of the edges as a third method for measuring distance. For these last two methods, the direction of the flow is not taken into consideration.

Quartiles are employed to divide a dataset into equal parts, such that the data is split into segments, each containing 25% of the total dataset [1]. This approach is utilized for the three distances used to compare the change in pressure.

4.5.2 Inflow and CBF calculation

The term inflow refers to the volume of blood per unit of time that enters the network, that is, the sum of the total incoming flows. This inflow is used for calculating the CBF, which has units of $\frac{ml}{min \cdot g}$. Therefore, the use of the brain tissue density is necessary to determine the network's mass in grams. This density is considered to be 1047 $\frac{kg}{m^3}$ [12], and the volume of the network is extracted using ParaView.

5. Implementation

In this section, we will delve deeper into the implementation carried out during the project. The most significant proposals and changes are discussed in Section 7.1.1 and 7.1.2 during the presentation of results. These changes were made to the cost function used in the algorithm during the simulations, as a result of the initial outcomes. Therefore, they are explained in the results section, since it is necessary to show the output of the simulations to understand the rationale behind these changes.

5.1 Preliminary study implementations

The primary implementations for this study included the automation of simulations to run consecutively, the addition of generation calculations to the existing code, and the classification of all bifurcations where blockages occur using a Python script.

5.1.1 Simulation automation

For both methods of inducing the microstroke, a loop was established so that when one simulation finished, the next one would start consecutively until all the simulations were completed. The aspect that changes in each method is the edge of the network where a blockage occurs. Therefore, initially, all network files are saved with the diameter of each edge (where the occlusion is to be induced) reduced by 99%. During the simulation, a loop is set up to sequentially read all these files as each simulation is conducted.

5.1.2 Generations

To calculate the generations using the definition adopted for this study, the process was integrated into the code where the simulations are carried out. An option was added for the user to choose whether a blockage is being simulated or not. If chosen, these generations are calculated, with generation 0 being the blocked capillary, generation 1 comprising the capillaries immediately connected to it, and so on, up to generation 4. Beyond this point, calculation ceases, and the remaining capillaries in the network that have not yet been assigned to any generation are considered to be generation 5.

- Initialize the generations list with -1 for all edges in the graph.
- Assign generation 0 to the blocked edge.
- For each generation from 1 to 4:
  - Create a temporary list to store edges for the next generation.
  - For each edge in the current generation's list:
    - Obtain the incident nodes of that edge.
    - For each incident node, obtain the incident edges.

        * If an incident edge does not have an assigned generation, assign the current generation to it and add it to the temporary list.
    - Update the edges list with the temporary list for the next iteration.
- Assign generation 5 to all remaining edges without an assigned generation.
- Create a dataframe with edge IDs and their generations.
- Save the dataframe to a CSV file.

5.1.3 Type of bifurcation

For the identification of each bifurcation where the blockage occurs, a Python script was used that follows the following logic:

- Initialize lists for different configurations of in and out flow at blocked edges (`_2_in_2_out`, `_1_in_2_out`, `_2_in_1_out`, `_1_in_1_out`).
- For each blocked edge:
    - Determine the flow direction based on baseline pressures at the nodes of the edge.
    - Identify incoming and outgoing neighbor nodes, excluding the direct connection of the edge.
    - Calculate the count of incoming and outgoing neighbors based on pressure differences.
    - Categorize the blocked edge into one of the lists based on the number of incoming and outgoing neighbors.

5.2 Final study implementations

It was in this study where the most significant changes of the investigation were carried out. However, these changes are explained in the results section, as previously mentioned.

5.2.1 Generations

Regarding the generations calculated for this study, the definition from Section 4.4.2 was used. Since there is only one blockage, ParaView was utilized to visualize the baseline simulation, and the assignment of generations was done manually, taking into account the direction of the flow.

5.3 Inflow and CBF

For the calculation of inflow and Cerebral Blood Flow (CBF), another Python script was used, and its logic can be summarized in the following points:

- Initialize an array to sum the inflows.

- For each set of flow rate, pressure, and BC pressure files:
  - Read the flow rate and pressure data from the files.
  - Create a mask based on the condition where BC pressure is greater than pressure at neighboring nodes.
  - Identify edge IDs corresponding to the BC-neighbor relationship.
  - Calculate the conditional sum of flows to obtain the inflow.
  - Store the inflow sum in the array.
- Input the dimensions of the network box to calculate its volume.
- Calculate the mass of the brain tissue in the network box using its volume and the density of brain tissue.
- Compute the CBF using the inflow data, converting units as necessary to obtain ml/min per gram.

6. Preliminary study

As explained in section 4.2, this preliminary study distinguishes two methods of inducing microstroke. In this section, the results obtained for both are presented, along with conclusions focused towards the final study.

6.1 Microstroke setup 1 - capillary occlusion and boundary condition tuning

In the following we explore the microstroke setup 1, i.e., the case where pressure boundary conditions are tuned for baseline and stroke. Additionally, for the stroke case the diameter of the occluded capillary is reduced by 99% and a 0 target velocity is added to that same capillary.

The subsequent inquiry revolves around the necessity of updating boundary condition values when employing this method to simulate the microstroke. If the solution varies significantly based on the microstroke's location, it could potentially influence the network's flow, which makes comparison of different time points more difficult.

Firstly, it is necessary to have the simulation under healthy conditions to compare with cases where blockage is induced. This simulation, referred to as the baseline, uses the 15 selected velocities as objective values and is carried out with $\gamma = 200$, an optimal value determined through the previous analysis.

The aim of this study is to induce stroke using 15 known velocities in the network and analyze whether the pressures in the nearby boundary conditions tend to undergo more significant changes than those farther away. Additionally, the goal is to investigate alterations in flow near the stroke, including changes in directions. To achieve this, the network is divided into generations, as explained in section 4.2.5. In addition, we will also analyze the influence of the local topology where the blockage occurs. That is, depending on the type of bifurcation where the occlusion occurs, we will analyze the changes that occur when occlusion happens in one type of bifurcation versus another. Based on the number of inflows and outflows to the block capillary, one type of bifurcation or another is defined [16].

Now we can proceed to induce the blockage in order to compare the results with the baseline simulation.

It is necessary to induce blockages at different locations in the network, since we want to compare the results based on the type of bifurcation. Thus, we randomly choose 20 blood vessels to block (one per simulation), ensuring that these are evenly distributed throughout the network, including both edges and the center of the network. Also, it is ensured that none of these edges are boundary edges. This way, the partial derivative $\frac{\partial J}{\partial \alpha_l}$ is 0 for all these cases to compute Eq. 28.

As explained at the beginning of this section, the stroke will be induced in two different ways: by tuning the pressure at the boundary conditions and by simply solving the forward problem. When tuning the boundary conditions, an additional target edge with a 0 velocity

constraint is added to the 15 random velocities picked earlier, apart from decreasing the diameter 99% of its in vivo value. The other method only solves the forward problem when the diameter is also reduced 99% of its value.

The results of tuning the pressures will be presented first. We will begin by displaying and analyzing the results through the relative change in flow corresponding to each generation. To do this, we used the formula for relative change as described in Eq 31.

Eq. 33 shows the relative change between the baseline a stroke simulation in order to compare how the different variables change.

$$rel_{change} = \frac{|q_{stroke} - q_{baseline}|}{|q_{baseline}|} \tag{33}$$

In Figure 22 the relative change calculated following Eq. 33 is used. This change is higher the closer it is to the occlusion. That is, the first generation tends to have a higher relative change value than the second and so on. This can be observed in the median, rather than the mean. This occurs because the median is less susceptible to being affected by outliers than the mean, as it is possible that there may be more change in some blood vessels further away than others closer to the occlusion. Furthermore, the farther away one is, the more blood vessels that generation encompasses (though not many blood vessels), so a high value may obscure this trend.

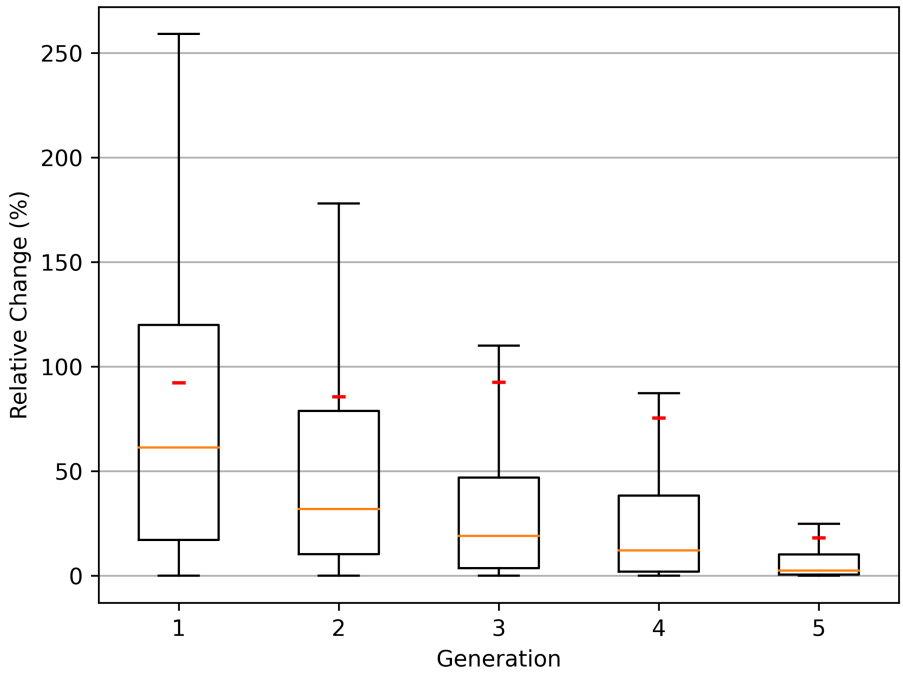

Figure 22: Boxplot with the flow rate relative change per generation. The red line represents the mean throughout all the simulation, and the orange line inside the box, the median.

On the other hand, delving deeper into the mean change observed in the first generation

across simulations with induced blockage reveals a remarkable disparity in the values, as it can be seen in Figure 23.

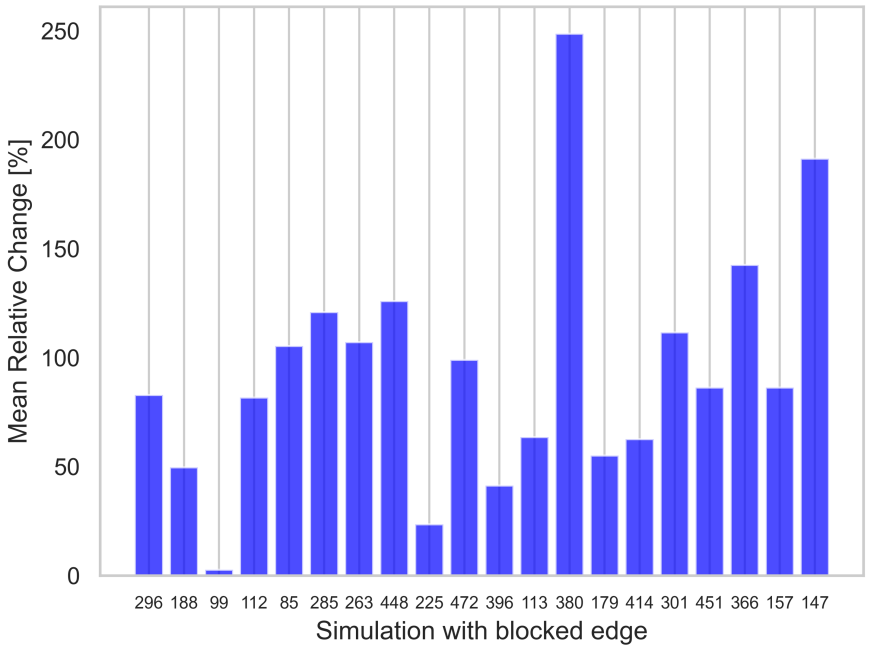

Figure 23: Mean relative flow change of the first generation for each simulation.

Indeed, this suggests that the variation might be highly influenced by the type of bifurcation where the blockage occurs. Therefore, a detailed analysis of this aspect will follow.

Out of the 20 simulations, we have representations of all types of bifurcations, albeit in varying numbers. Consequently, the mean flow direction changes were calculated for each type of bifurcation across the network's vessels. This is depicted in Figure 24.

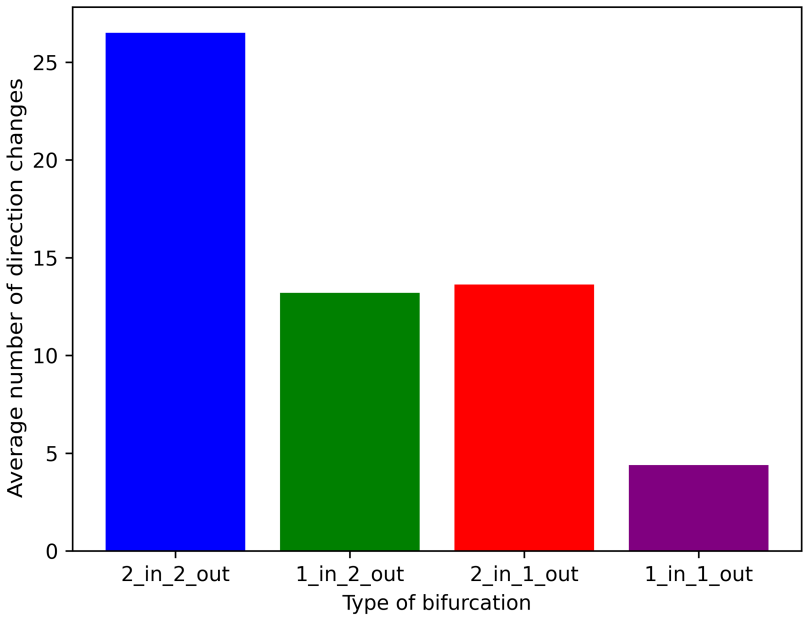

Figure 24: Mean number of direction changes in the whole network per type of bifurcation.

Among the 20 randomly selected blocked edges, two are of type 2-in-2-out, five are 1-in-1-out, another five are 1-in-2-out, and eight are 2-in-2-out. As observed, the 2-in-2-out bifurcation type induces the most significant flow direction changes and consequently has the most impact on flow in the event of a blockage.

Now, we proceed to analyze the change in boundary pressure concerning the distance to the blockage. Firstly, using a specific case.

To do this, two simulations with blockages are selected: one with the blocked blood vessel near the edge of the network and the other in the middle. Additionally, two boundary nodes near the simulation with occlusion near the edge are chosen. In this way, the pressures obtained with blockage in these two boundary nodes are compared to the baseline simulation (healthy conditions). Boundary nodes 12 and 34 are picked since they are both close to the edge blocked in the border of the network and also are distant in the network from the other block edge chosen. The following image shows the locations of the vessels and boundary conditions.

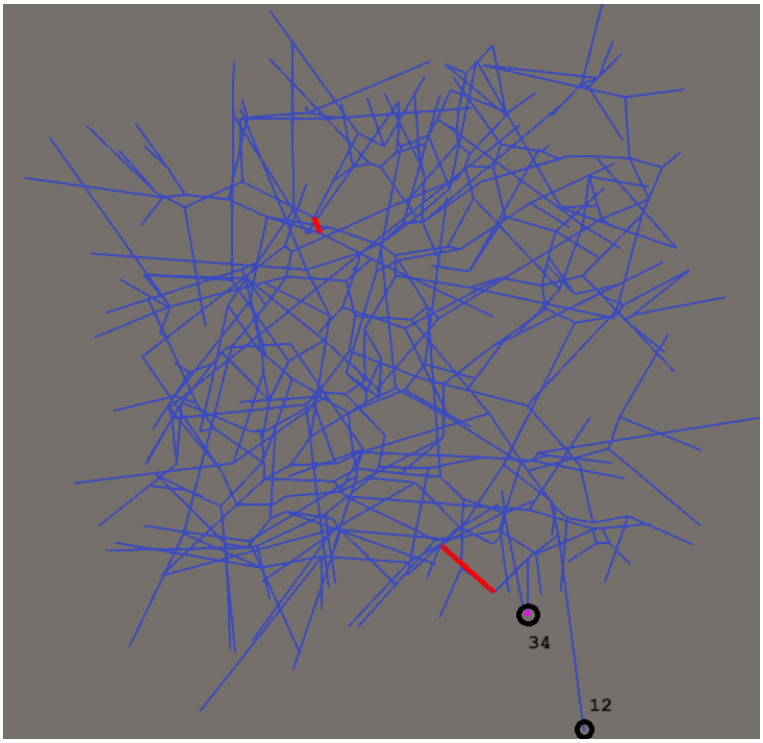

Figure 25: The red edges are the ones chosen to be blocked to compare the pressure change of boundary nodes 12 and 34 (which are close to one of the blocked edges).

The results of this are shown in Figure 26, depicting the evolution of pressure for the baseline simulation (initial), the one with occlusion near the boundary (near BC), and the one in the center. The same graph is created for both boundary nodes.

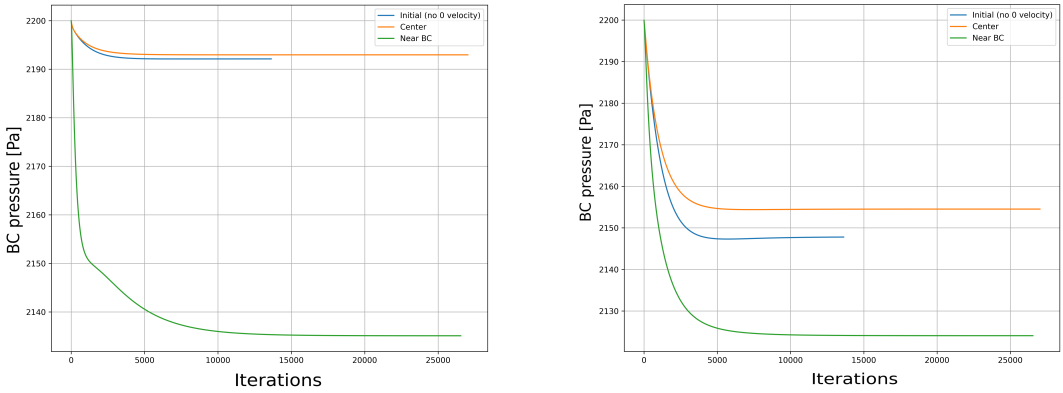

(a) (b)

Figure 26: (a) Pressure change in boundary node 34 adding the occlusion near the border and in the center (b) Pressure change in boundary node 12 adding the occlusion near the border and in the center.

Once again, we utilize the same 20 simulations. Distance is computed in three different ways for this analysis: Euclidean distance, number of edges, and sum of the lengths of edges in

the shortest path. For the first method, we utilize the coordinates of the midpoint of the blocked vessel. For the latter two, we use the shortest path from the nearest node in terms of edge count to each boundary node.

For this purpose, the data is divided into quartiles to group the three types of distances into ranges, separately. These are then depicted in the following graphs.

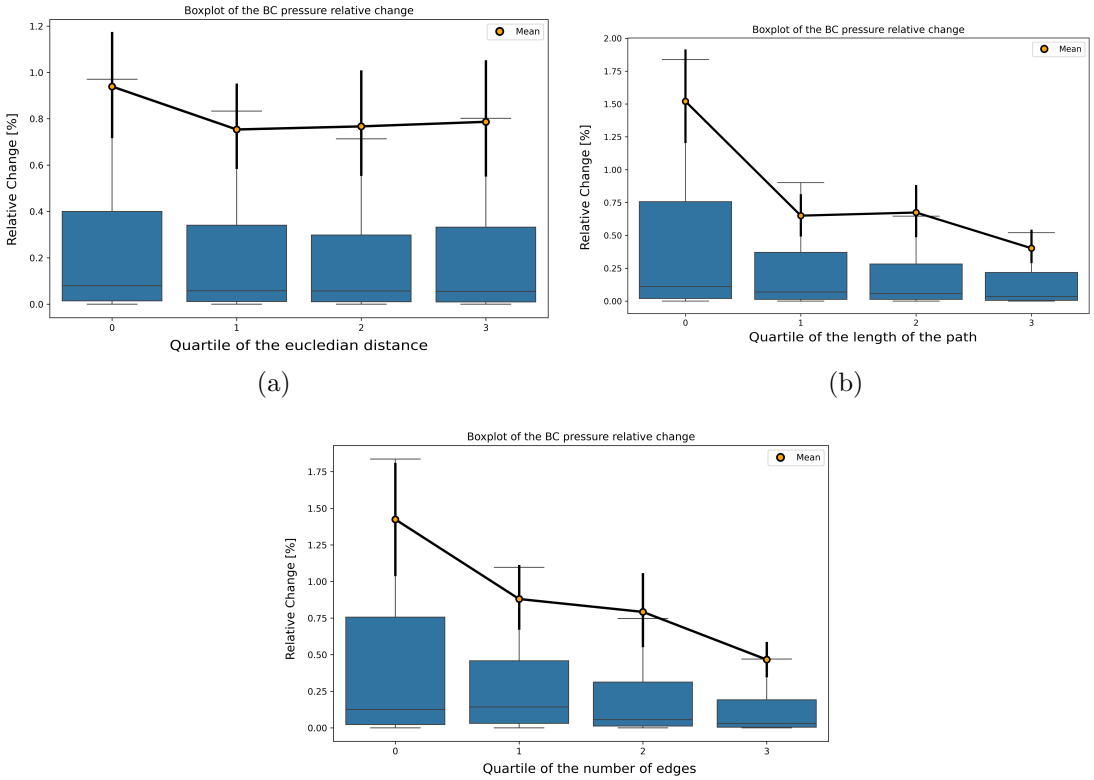

Figure 27: (a) Eucledian distance (b) Sum of the lengths of the shortest path and (c) Number of edges.

Clear trends are only evident for a higher change in the mean relative pressure change using the number of edges in the shortest path. There is also some indication of this trend for the median relative change using the sum of lengths of the shortest path.

As expected, there is a greater change in flow the closer it is to where the blockage is induced. The change in pressures should be compared with a distance that refers to the network, not the Euclidean distance. Furthermore, this method has confirmed that the type of bifurcation where the microstroke is induced takes on vital importance.

6.2 Microstroke setup 2 - capillary occlusion only

In this section, the microstroke is not induced by tuning the boundary conditions. Instead, the diameter is reduced by 99%, and directly, with the solution obtained from the healthy simulation, the forward problem is solved. The following steps are carried out:

Given that the boundary conditions remain constant throughout this approach, the analysis focuses solely on the variations in flow within different generations and the alterations in direction contingent upon the specific type of bifurcation. Commencing with an examination of the generations as shown in Figure 28:

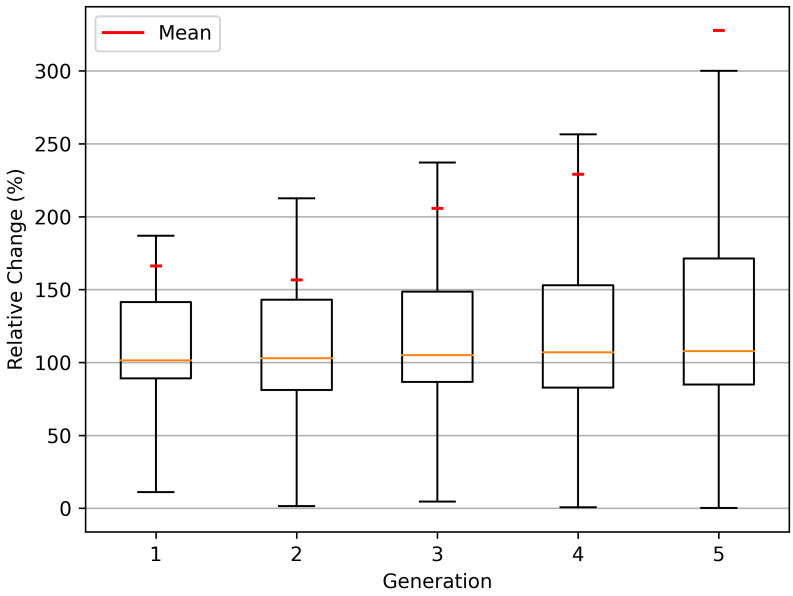

Figure 28: Boxplot with the flow rate relative change calculated following Eq. 31 per generation.

In contrast to tuning the boundary conditions, this method of inducing the blockage, the changes in the flow rate are higher than using the other method. However, there is no dependence in function of generations. Furthermore, the observed changes are more substantial compared to the previous scenario.

Similarly, the changes in flow direction according to the type of bifurcation show consistent results. The mean changes in direction obtained are nearly identical across the different topologies as it can be seen in Figure 29.

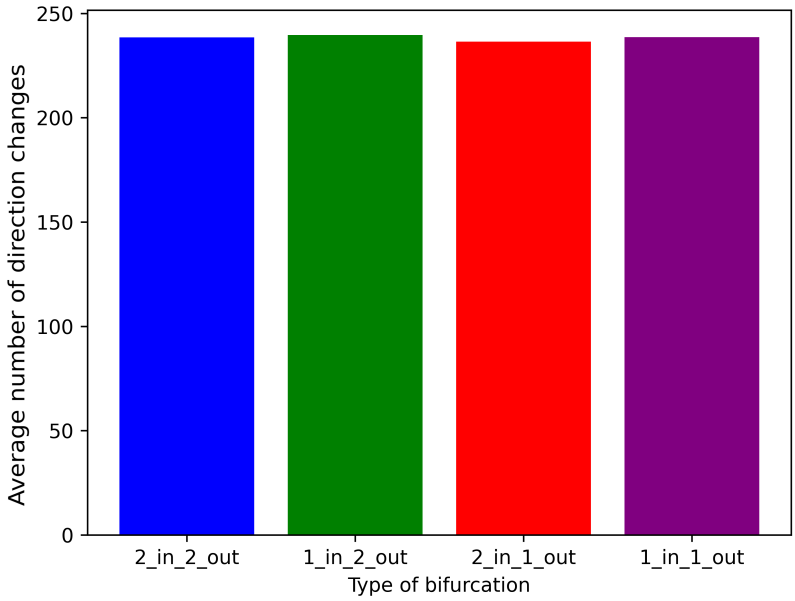

Figure 29: Mean number of direction changes depending on the type of bifurcation.

Finally, in Figure 30, the difference in inflow (i.e., the summed inflow over all boundary nodes) in the network for the different simulations is depicted. As observed, while tuning the boundary conditions once a velocity target value of 0 is added, a similar inflow to that of the baseline simulation is obtained. However, the same does not occur when the diameter of the blocked capillary is decreased.

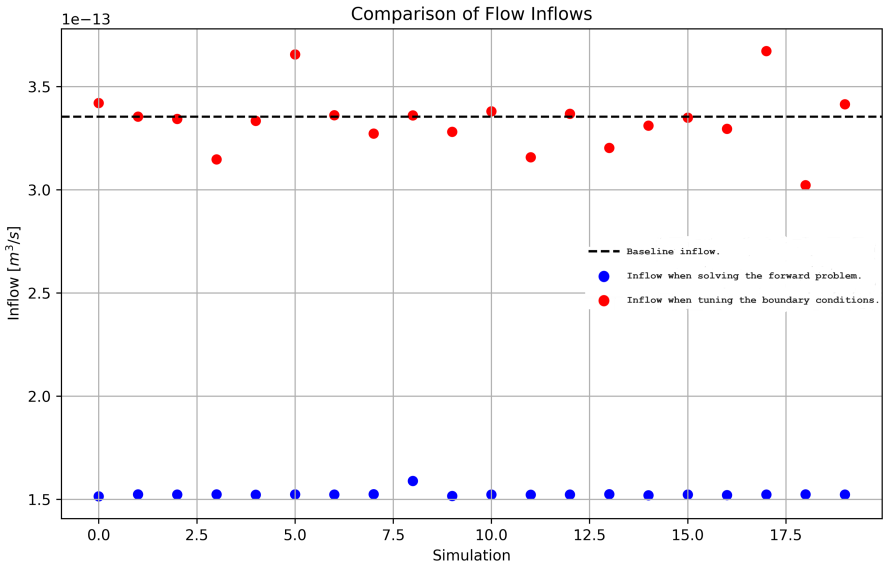

Figure 30: Summed inflow over all boundary nodes comparison for the baseline simulation and the simulations keeping constant the boundary conditions and tuning them.

This method of inducing the microstroke contradicts the study conducted in [19], as it does

not show a greater change depending on the type of bifurcation where the microstroke is induced. Moreover, the changes observed in the flow are too high compared to what is expected in a correct induction of the occlusion.

6.3 Conclusions

From the preliminary results presented in this study, valuable conclusions can be drawn to better understand the events occurring during a blockage. These conclusions also provide insights to consider in the final study. They include:

1. Given the obtained results (Figures 29,28), the second method presented for inducing occlusion seems to be invalid. Solving the forward problem after reducing the diameter of the blocked edge completely alters the flow field. Therefore, the results show no trend in change with the generations or with the type of bifurcation. Some changes are always expected when inducing the microstroke (for both cases). However, not tuning the boundary conditions makes them relatively large. Consequently, we deduce that the first method presented, in which the boundary conditions are tuned, will be used in the final study to induce the microstroke.

2. Tuning the boundary conditions did induced the microstroke properly. However, this study has the limitation that the same velocities as the baseline simulation are still being used as target values to induce the stroke. This could slightly alter the results, as we expect changes in flow, albeit small (depending on the distance to the occlusion), in the rest of the vessels in the network when a blockage occurs.

3. Although there is a greater change in flow rate with the first generations, this trend is not entirely clear. Additionally, the average change in flow in the first generation varies greatly in each simulation. Therefore, a study was conducted based on the type of bifurcation, focusing on the direction changes presented. Depending on the type of bifurcation in which the microstroke occurs, we will have significantly different number of direction changes in the network. Furthermore, the results indicate that for future studies, it is necessary to divide the generations into downstream and upstream. Figure 23 shows very different mean relative change for the different simulations, so apart from the importance of the local topology, it is expected to have different change upstream than downstream.

4. Regarding the change in pressure at the boundary conditions relative to the distance to the stroke, it has been shown that it changes more the closer the boundary condition is to the occlusion. However, the Euclidean distance should not be used, but rather a distance referenced to the network.

5. There is a strong trend in the change of pressure at the boundary conditions as a function of distance (referred to the network, not the Euclidean) as shown in Figures 27(c) and 27(b). Also, if we take a look to a specific case, it can be seen how the boundary conditions near the microstroke varies its values much more than when the boundary condition is far from the microstroke.

6. Although the pressure change is bigger in the boundary conditions near the microstroke,

it is not a very big change. The biggest changes occur as outliers that are not as close to the blocked capillary. This can be explained by the fact that the flow direction is not taken into account when calculating the distance between the microstroke and each boundary.

7. Results

In this section, we will present the results obtained for the final capillary network used in the actual study. We will explain the process undertaken to obtain the results and discuss the changes made in the inverse problem to achieve more physiological and definitive results than the initial ones. Note that in the realistic network two target velocities are directly at the boundary. However, this has currently been neglected and $\frac{\partial J}{\partial \alpha_l}$ is assumed to be 0.

7.1 Excluded measurements

Despite the exclusion of the measurements due to the mass balance error, the initial results obtained were non-physiological (i.e., very high and low RBC velocity, pressure drop in the whole network), indicating that the solution obtained is not representative of a situation as realistic as possible. Table 6 shows the parameters used to carry out the first simulation for normal healthy conditions. For this simulation and all the presented in this study, the derivative $\frac{\partial J}{\partial \alpha_l}$ is considered 0.

Table 6: Parameters baseline 1

Gamma	**Targets**	**Targets reached]**	**Threshold**	σ	**Iterations**
2000	19	19	0.2	Target value	35461

"Threshold" refers to the error, expressed as a percentage, allowed when determining whether a target value has been reached. In this case, it is set to 0.2, meaning that the obtained value can be up to 20% higher or lower than the target value. This simulation was stopped when all the targets values are within the threshold.

Table 7: First baseline results summary

Simulation	Baseline 1
Excluded measurements	228,162,122,264
Pressure drop [mmHg]	114.9
CBF	1.2
Cost function	Measurements
RBC velocity median [mm/s]	2.17
RBC velocity std deviation [mm/s]	16.13
Vessels outside of the range	69

As a reminder, the cost function "measurements" refers to the one presented in Section 2.4.1.

Although the CBF value falls within the normal physiological range, we observe a significant difference in pressure. Based on the results presented in [16], the average pressure drop across the capillary bed should be around 50 mmHg. However, larger pressure drops of approximately 80 mmHg might be possible considering we are close to cortical surface and both large arteries and veins are present.

Furthermore, the ideal scenario would be to obtain all red blood cell velocities between 0.05 and 10 mm/s to consider the solution physiological. However, if we examine the distribution of these velocities for this solution, we find many vessels outside of this range, with extremely high values.

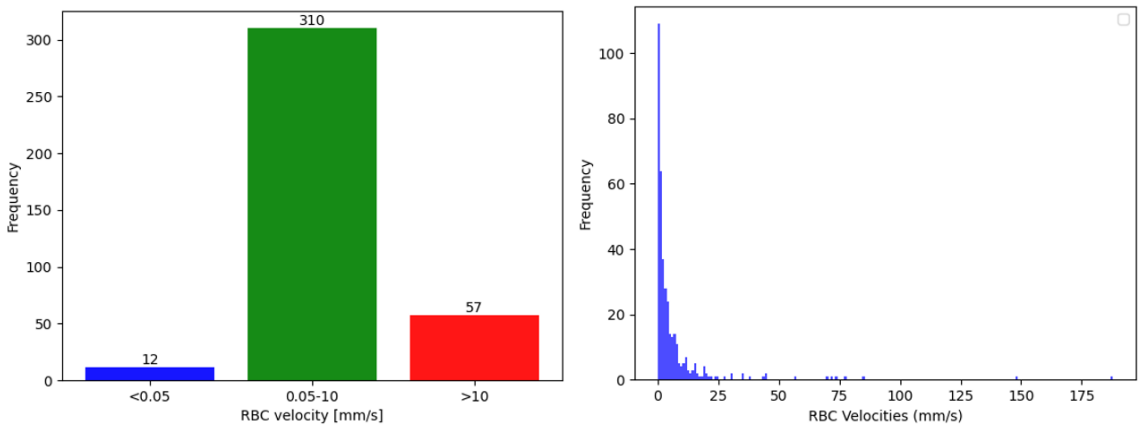

(a) (b)

Figure 31: (a) Bar plot showing the number of vessels within and outside the range (b) RBC velocity histogram

7.1.1 New cost-function to obtain physiological RBC velocities

For this reason, it was necessary to modify the cost function in order to achieve a more physiological solution. Thus, it was decided to add a term to the initial cost function for the remaining vessels in the network. This term forces the system to ensure that all vessels have a red blood cell velocity within the previously mentioned range. The cost function is now defined as follows:

$$J_{ranges}(\nu) = (1-\omega)\cdot n_{ranges}\sum\left(\frac{u^{\nu}_{rbc_t} - u_{rbc_t}^{\text{target}}}{\sigma_{target}}\right)^2 + \omega\cdot n_{targets}\sum\left(\frac{|u^{\nu}_{rbc_t}| - u_{rbc_t}^{\text{ranges}}}{\sigma_{ranges}}\right)^2 \tag{34}$$

With ω being the weight given to the range term. Each term is multiplied by the number of vessels of the other term to make them equally important since the target term comprises 19 capillaries, and the ranges term 360. The value of σ_{ranges} used is the midpoint of the given range, in this case 4.995e-3$\frac{m}{s}$, since the code operates in SI units. σ_{ranges} has the same values as the target velocities of each capillary. This cost function will be referred to as the "ranges" cost function from now on.

As a consequence of this change, now the derivative $\frac{\partial J}{\partial \alpha_l}$ is not zero. It is different from zero in vessels that are boundaries, as the pressure of the boundary node appears in the definition of the RBC velocity. This derivative is neglected and considered zero for the simulations in the present study.

To carry out these simulations, the terms were switched on sequentially. That is, first the initial cost function was used to achieve all target values, and then starting from that solution, the cost function presented in Eq. 34 was used. This approach yielded better results than using this cost function with the range terms initially. Tables 8 and 9 show the parameters used for these simulations and the most relevant results, respectively.

Table 8: Parameters used in baseline trial simulations. The value of gamma starts from 20 and it increases 10 every 2000 iterations.

	Baseline 2	**Baseline 3**	**Baseline 4**
Gamma	20+10	20+10	20+10
Targets	19	18	17
Targets reached	17	17	17
Threshold	0.2	0.2	0.2
Iterations	45000	50000	75000

Simulations Baseline 2 and 3 are manually stopped as not all target values are reached. Before this, the cost function becomes completely flat, as well as the pressure values at the boundaries. Simulation Baseline 4 is also manually stopped. Despite reaching all target values, not all vessels are within the range. Therefore, it is also stopped following the same criteria as the previous ones.

Table 9: First results using the ranges cost function summary

Simulation	Baseline 2	Baseline 3	Baseline 4
Excluded measurements	228,162,122,264	228,162,122,264,341	228,162,122,264,341,75
Pressure drop [mmHg]	126.2	77.5	75.9
CBF	0.21	0.18	0.11
Cost function	Ranges	Ranges	Ranges
RBC velocity median [mm/s]	1.6	1.61	1.21
RBC velocity std deviation [mm/s]	3.81	2.8	2.31
Vessels outside of the range	46	28	18

As shown in Table 9, the results improve by excluding two additional measurements, 341 and 75. One of them is located in a region of the network that was challenging to extract from

the segmentation. It is an area where individual capillaries cannot be clearly distinguished, which may have led to errors in creating the network or in measuring the experimental velocity. The other measurement requires an extremely large pressure change for a single capillary, indicating a likely error. Therefore, these two measurements were also not used as target values.

These simulations were carried out sequentially as well; first, the target values were achieved using the initial cost function, and once achieved, that solution was used to initialize the simulation with the cost function that includes the range term.

With the aim of demonstrating the fulfillment of convergence conditions for the simulations, the pressure values at the boundaries and the value of the cost function with the iterations are shown in Figure 32 for Baseline 4 simulation.

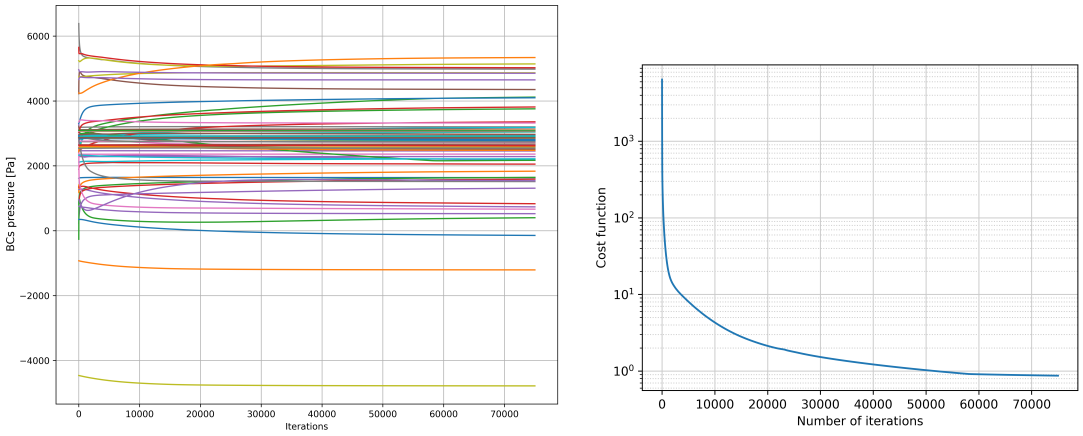

(a) (b)

Figure 32: (a) Boundary conditions throughout the iterations (b) Cost function value throughout the iterations.

7.1.2 New cost function to obtain a physiological pressure drop

In addition to the cost function change explained in the previous section, there was also consideration given to adding a term to minimize the change in pressure values across all boundaries. Thus, the cost function would be:

$$J_{ranges}(\nu) = (1-\omega)\cdot n_{boundaries}\sum\left(\frac{u^{\nu}_{rbc_t} - u^{\text{target}}_{rbc_t}}{\sigma_{target}}\right)^2 + \omega\cdot n_{targets}\sum\left(\frac{P^{\nu}_{sim,l} - P^{initial}_{l}}{P^{initial}_{l}}\right)^2 \tag{35}$$

where $P^{initial}_{l}$ represents the initial pressure values of the problem, $P^{\nu}_{sim,l}$ denotes the simulated value at each iteration ν, and $n_{boundaries}$ is the number of boundary conditions.

Table 10 shows the parameters used for the simulation carried out employing cost function from Eq. 35.

Table 10: Parameters baseline 5. Gamma starts with a value of 50 and it increases 20 every 2000 iterations.

Gamma	**Targets**	**Targets reached]**	**Threshold**	ω	**Iterations**
50+20	19	11	0.2	0.3	20926

In this way, the pressure change is reduced, but as can be seen in Table 11, the target values are still not achieved. It appears that such a small pressure change is not feasible to attain the desired RBC velocities.

Table 11: Results using the new cost function to obtain a physiological pressure drop.

Simulation	Baseline 5
Excluded measurements	228,162,122,264
Pressure drop [mmHg]	56
CBF	0.48
RBC velocity median [mm/s]	1.31
RBC velocity std deviation [mm/s]	6.76
Vessels outside of the range	38

Therefore, the chosen cost function to employ is the one called "ranges." This allows us to achieve the RBC velocity measurements while obtaining a solution as physiologically accurate as possible.

7.2 Baseline simulation

In this section, we present the results obtained for baseline simulation 4, as it yielded the best and most physiologically plausible outcomes. Let us commence with the graphical representation indicating the achievement of all target values within the predefined threshold of 0.2. Figure 33 shows the RBC velocities before the simulation and after solving the inverse problem.

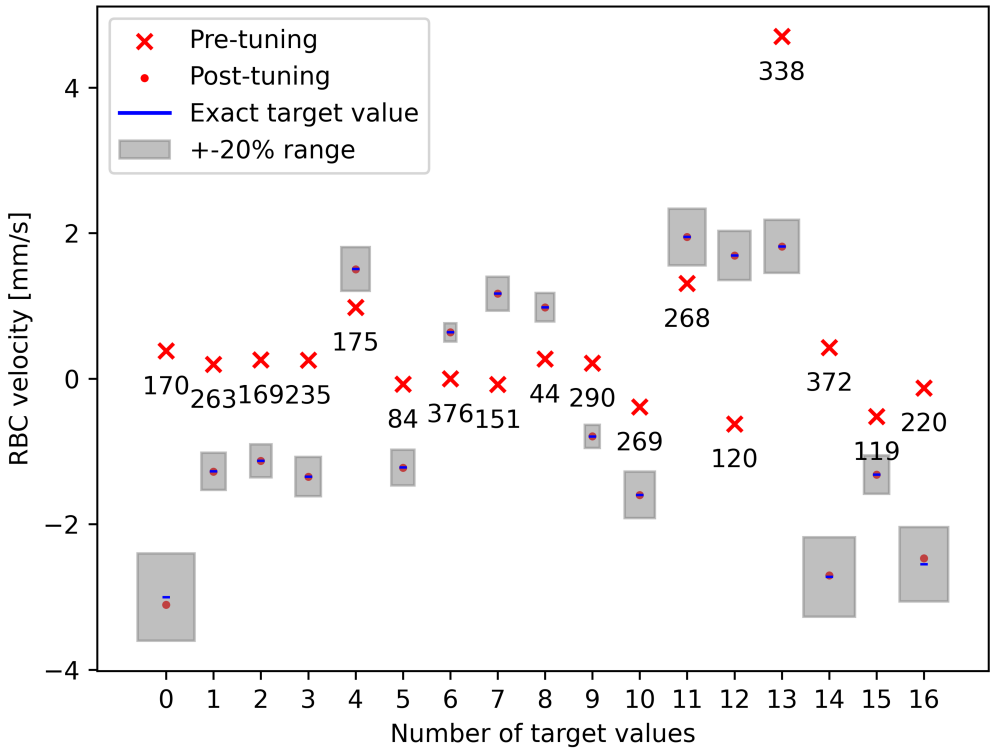

Figure 33: Pre-tuning and post-tuning target values for the baseline simulation.

It can be observed that these values have been attained with minimal error, as they are all closely situated near the exact value within the box representing the range. Upon observing the pressure histogram in Figure 34, negative pressures are apparent. Physically, this lacks meaning. However, they can be manipulated since what is of interest in this case, determining the flow rate and red blood cell velocity, is the pressure difference. Therefore, raising all pressures by a certain number would yield an equivalent solution without negative pressures.

In Figure 34, the pressure distribution for the boundaries in the network can be observed.

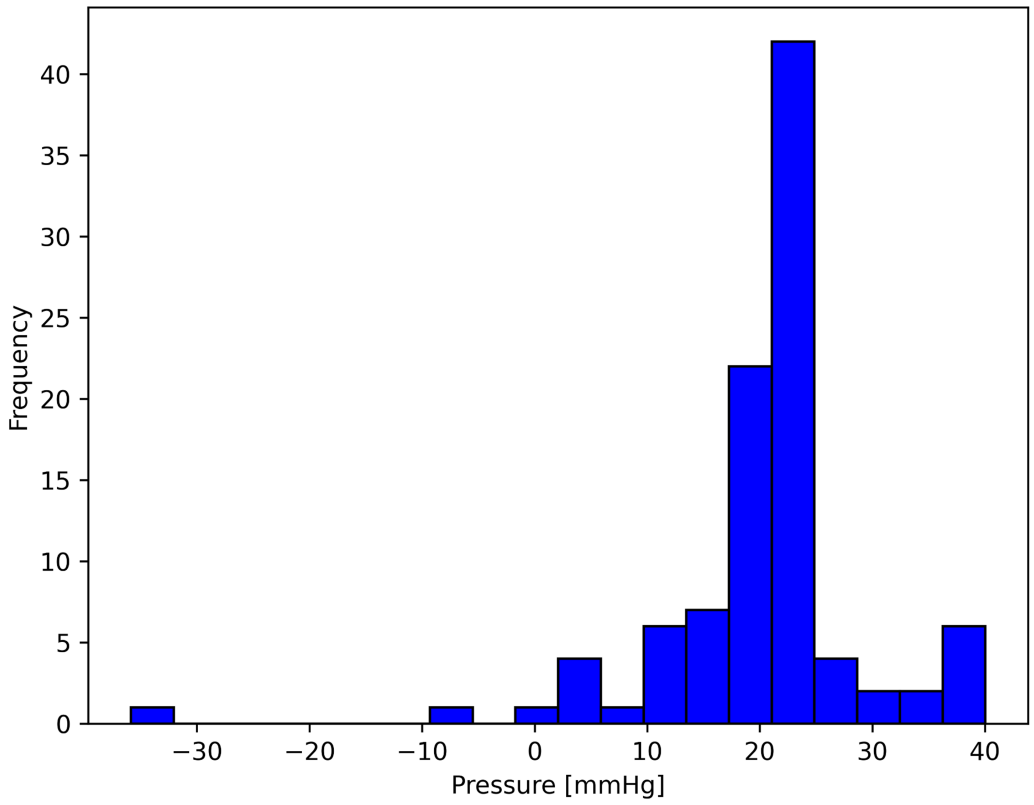

Figure 34: Boundary condition pressure histogram for baseline simulation.

Furthermore, it is evident that there are two outliers with significantly low pressure values, contributing to a higher pressure difference in the network. If we analyze Figure 35, we can observe the number of vessels above and below the range of RBC velocity, as well as the histogram of these velocities.

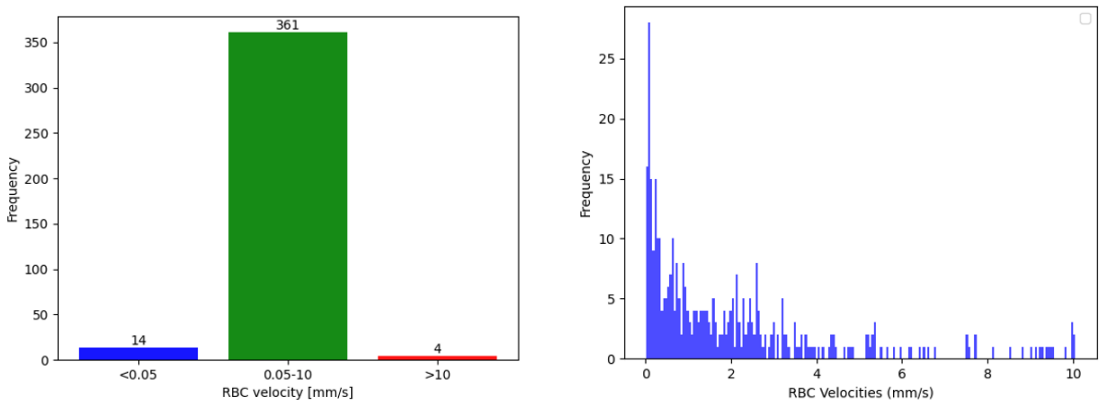

(a) (b)

Figure 35: (a) Bar plot showing the number of vessels within an outside the range (b) RBC velocity histogram.

Examining the histogram in Figure 35, it is apparent that the four values exceeding 10 mm/s are extremely close to this threshold. Comparing these results with those obtained in Baseline 1, a significant improvement is evident. In Baseline 1, we had 57 vessels exceeding 10 mm/s, with values reaching around 180 mm/s. Additionally, the pressure difference was 114.9 mmHg, whereas now it is 75.9 mmHg.

The following plots illustrate how the pressure values have changed at each boundary, categorized by the type of blood vessel (vein, artery, or capillary).

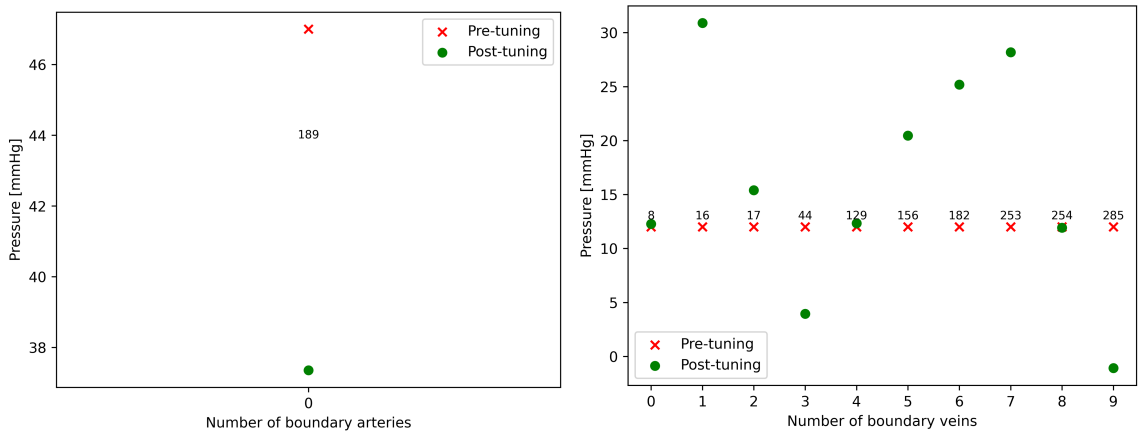

(a) (b)

Figure 36: (a) Artery pressure value pre-tuning and post-tuning (b) Veins pressure value pre and post tuning.

In Figure 37, the same outliers observed in the pressure histogram are depicted. These two values significantly decrease compared to the rest of the capillaries, resulting in a much higher pressure difference across the network.

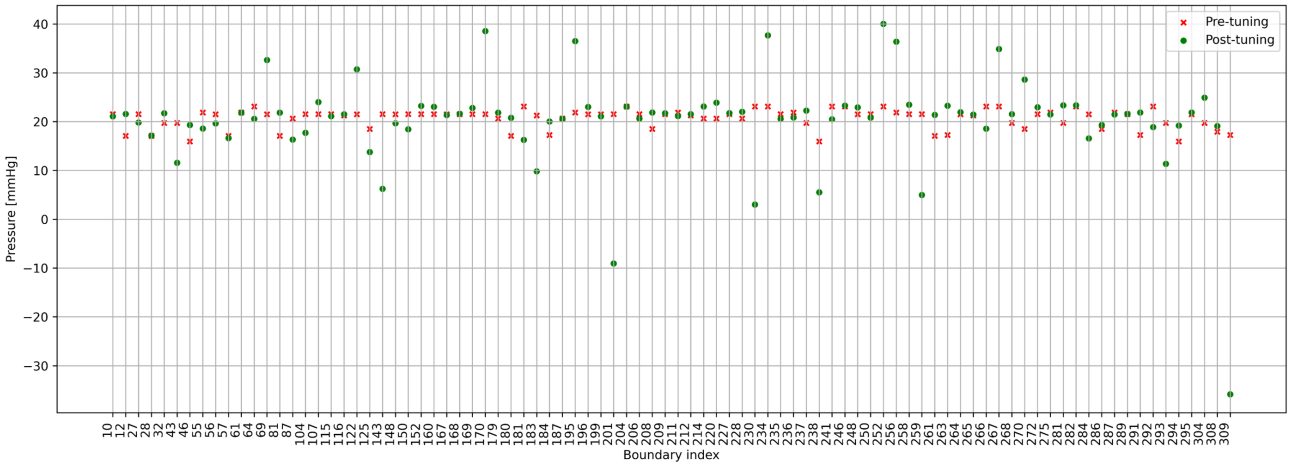

Figure 37: Capillaries pressure value pre and post tuning.

7.3 Induced Microstroke Simulation

Finally, the results obtained for the time point at which the stroke is induced are presented. Here, again, the process is carried out sequentially. First, the solution from Baseline 4 is taken, and the initial cost function is used to achieve all the target values. However, here, the diameter of the blocked edge is reduced by two orders of magnitude to ensure a very low velocity and to properly simulate the blockage. Subsequently, once again, this solution is used to initialize the simulation in which the cost function with the range term is utilized.

As can be seen in figure 38, the type of bifurcation we have at the blocked capillary is of the 2-in-1-out type.

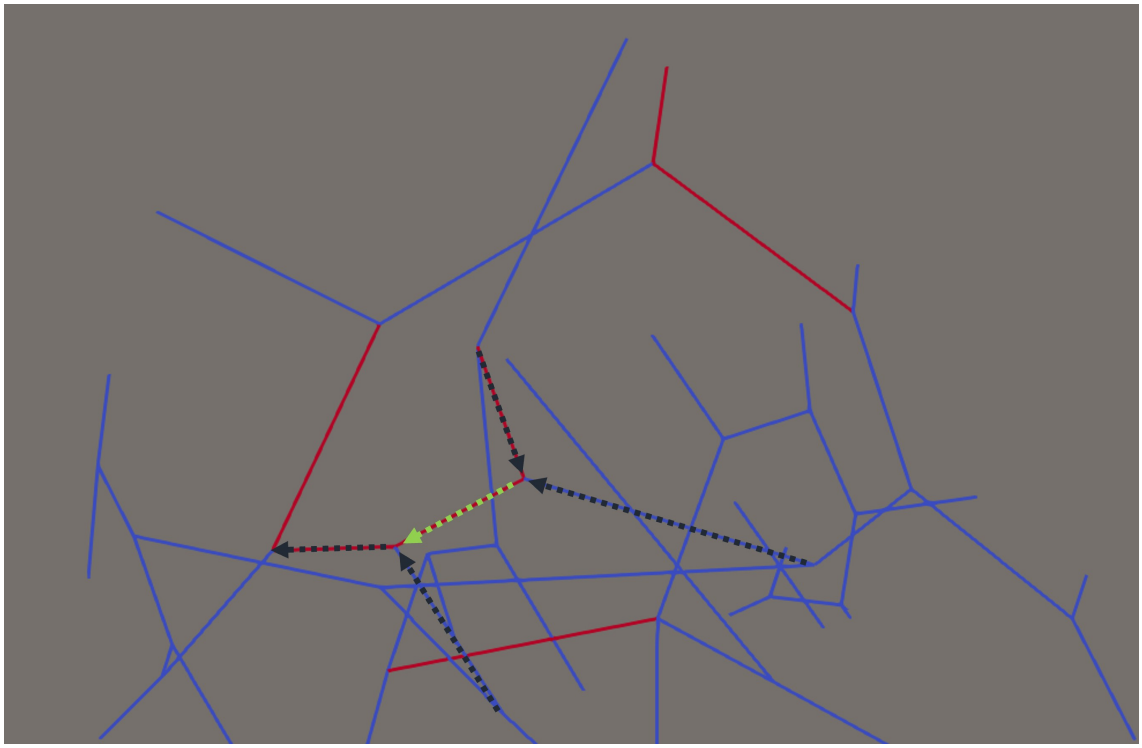

Figure 38: Representation of the flow direction in the occluded bifurcation during normal conditions without the microstroke.

Table 12 shows the parameters used for the stroke time point simulation and 13 shows the results obtained.

Table 12: Parameters used in stroke simulation

Simulation	**Gamma**	**Targets**	**Targets reached**	**Threshold**	**Iterations**
Stroke 1	20+10	16	16	0.2	180000

Similarly to the previous baseline cases presented, the simulation is stopped following the same criteria.

Table 13: Results inducing the microstroke.

Simulation	Stroke 1
Excluded measurements	28,162,122,264,341,75
Pressure drop [mmHg]	118.4
CBF $[\frac{ml}{min \cdot g}]$	0.15
Cost function	Ranges
RBC velocity median [mm/s]	1.33
RBC velocity std deviation [mm/s]	2.8
Vessels outside of the range	33

It can be observed from the tables that the pressure difference in the network increases significantly when the stroke is induced. Additionally, there is also a higher number of vessels outside the range of RBC velocities. We proceed to analyze the results more thoroughly through the generated graphs.

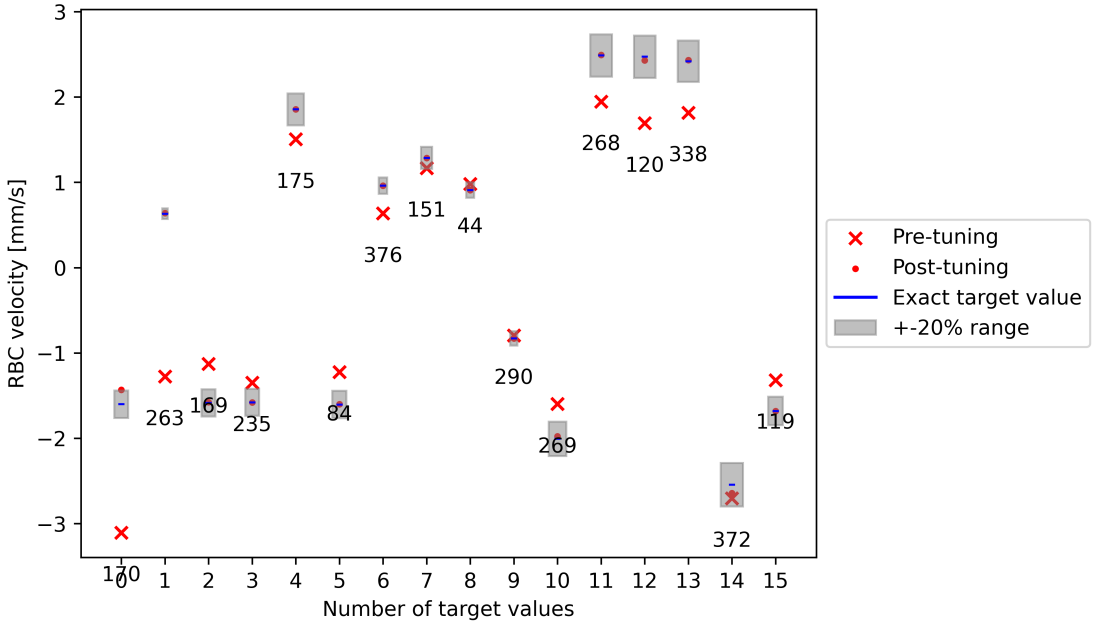

Figure 39: Pre-tuning and post-tuning target values for the stroke simulation.

All target values are reached; however, achieving the target for edge 170 is particularly challenging as it is right at the limit.

Once again, similar to what occurred in the baseline simulation, we have an outlier that significantly increases the pressure difference in the network. However, not taking it into account, we can observe how the distribution of pressures changes, becomes slightly wider.

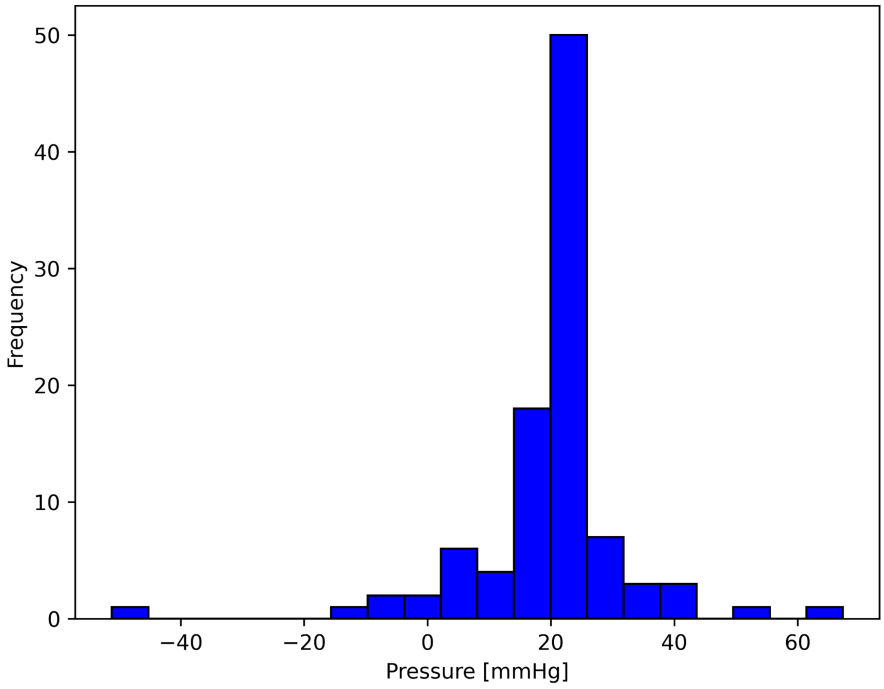

Figure 40: Boundary condition pressure histogram for stroke simulation.

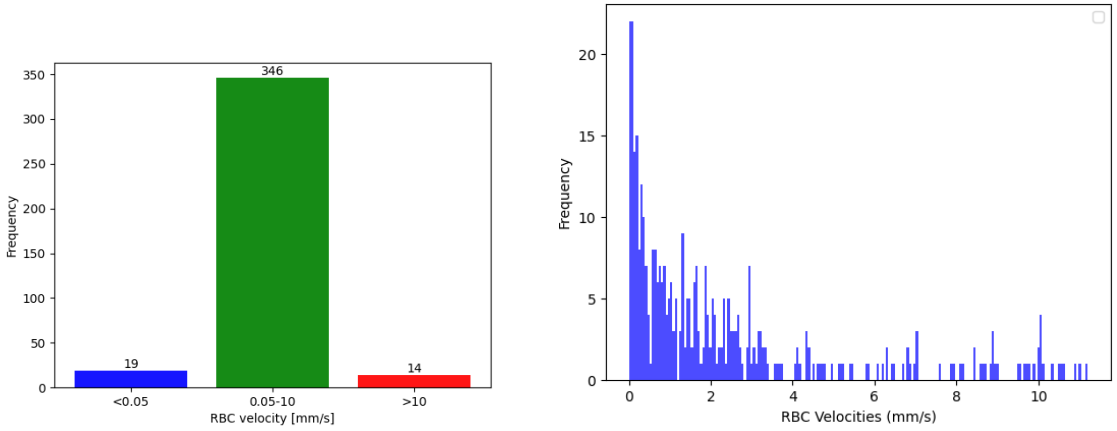

(a) (b)

Figure 41: (a) Bar plot showing the number of vessels within an outside the range (b) RBC velocity histogram.

For this simulation where we induce the occlusion, it is more challenging to achieve the desired range of velocities for all vessels. We have more vessels outside the range, although values above 10 mm/s are still quite close to this threshold. These values, as well as the low values below 0.05 mm/s, are likely caused by the induction of the blockage.

7.4 Baseline-stroke comparison

Let's proceed to analyze and compare the two simulations: baseline 4 under healthy conditions and Stroke 1 after inducing the stroke. This comparison is the main objective for which this study is carry out.

The main changes between the simulation with induced stroke and the baseline can be summarized in the following table:

Table 14: First results using the new cost function summary (transposed)

Simulation	Baseline 4	Stroke 1
Direction changes	-	38
CBF $[\frac{ml}{min \cdot g}]$	0.11	0.15
Pressure drop [mmHg]	75.9	118.4
RBC velocity median [mm/s]	1.33	1.21
RBC velocity std deviation [mm/s]	2.8	2.31
Vessels outside of the range	18	33

As can be seen, the CBF slightly increases in Stroke 1, indicating that the inflow also increases slightly. This means that more blood enters the network compared to the simulation under healthy conditions, which is consistent with the increased pressure drop.

To analyze the changes produced around the stroke, the generations were again used, this time dividing them into downstream and upstream. Only up to the fourth generation was calculated, beyond that point no generations are considered. This is shown in Figure 42.

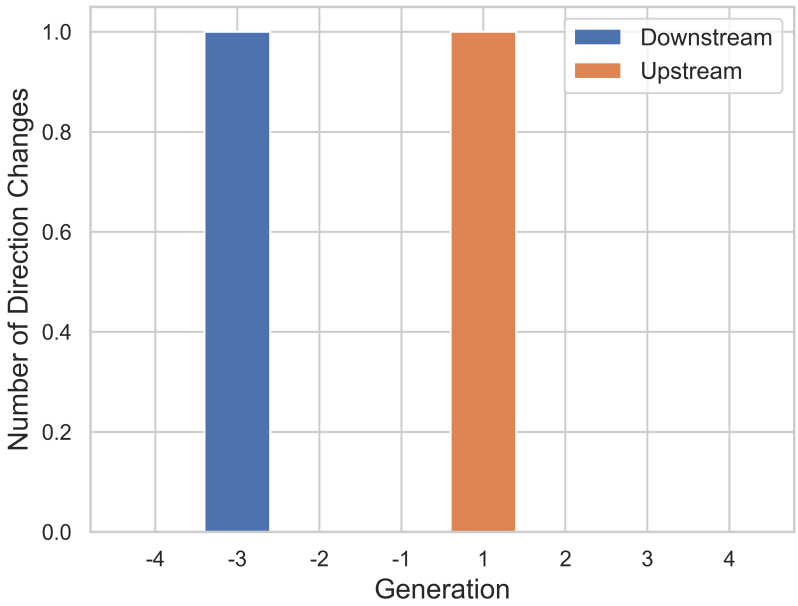

Figure 42: Direction changes in each of the downstream and upstream generations.

There is only one vessel per generation, except for generations 1 and 2 upstream, where there are two in each of these generations. Out of the 38 changes in direction compared to the baseline, only 2 occur in the calculated generations. Only one change in direction happens in the upstream generation, due to it being a type of bifurcation 2 in 1 out. This means that the downstream change in direction do not occur immediately in the nearby capillaries, but rather occur in generations 3.

Again, the definition of relative change from Eq. 31 is used to observe the change in flow rate across generations. This relative change do not show the direction changes, just the absolute difference in the values.

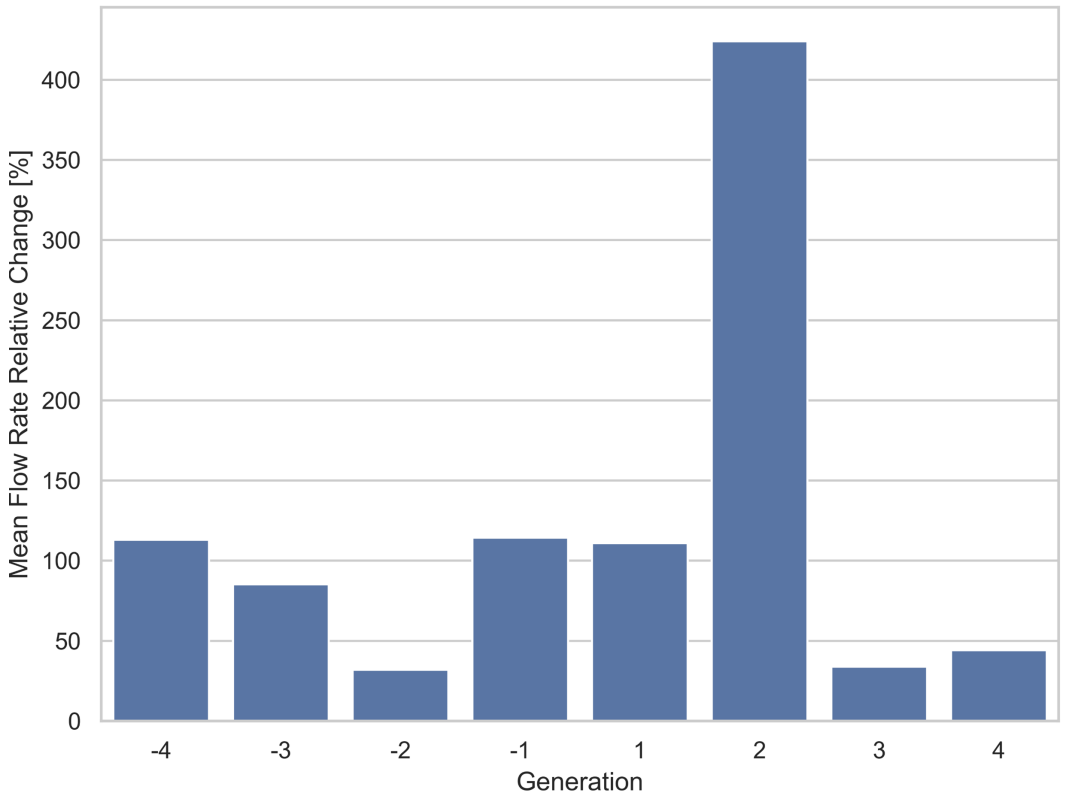

Figure 43: Mean flow rate relative change with respect to the baseline 4 simulation.

We might expect a greater change in flow rate in the first generations and in those where changes in direction occur. However, the greatest change occurs in the second upstream generation. This is because before the blockage, the flow entered from both capillaries adjacent to the blocked one. However, upon the blockage of one of these capillaries in the first upstream generation, the flow has to change direction, leading to larger changes in the second upstream generation, where a significant portion of the flow change is concentrated.

Inducing the stroke results in significant changes, especially in flow rate and red blood cell velocity as shown in Figure 44. The pressure at the boundary conditions changes very little in most cases, as it can be seen in Figure 45. Nevertheless, there are several boundaries that experience substantial changes in pressure, leading to a high mean but not median value. These changes cause a substantial alteration in flow rate and red blood cell velocities in the network.

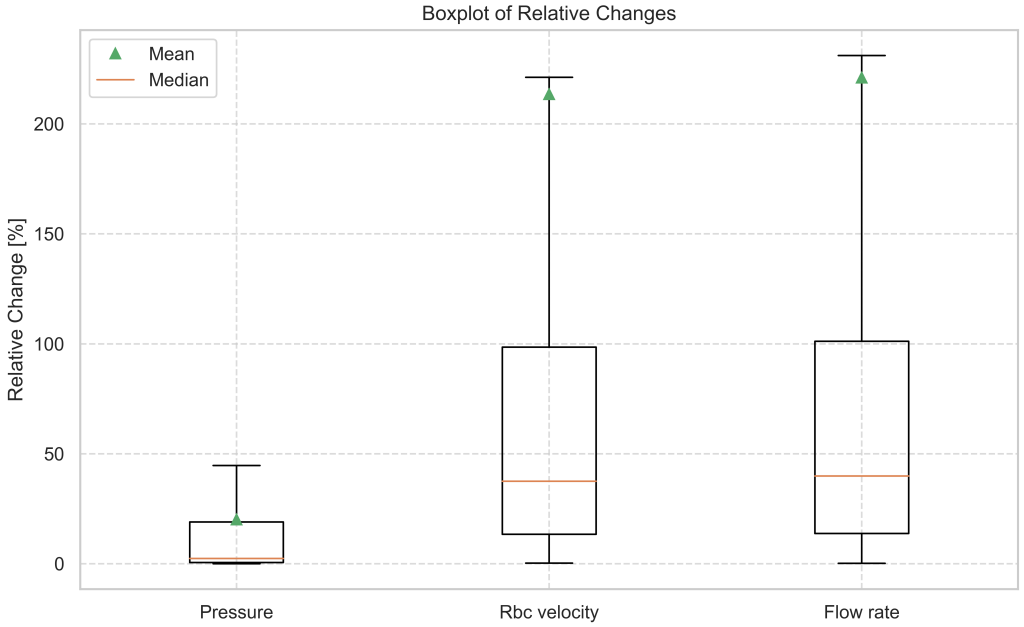

Figure 44: Boxplot for the pressure, flow rate and red blood cell velocity relative change with respect to baseline 4.

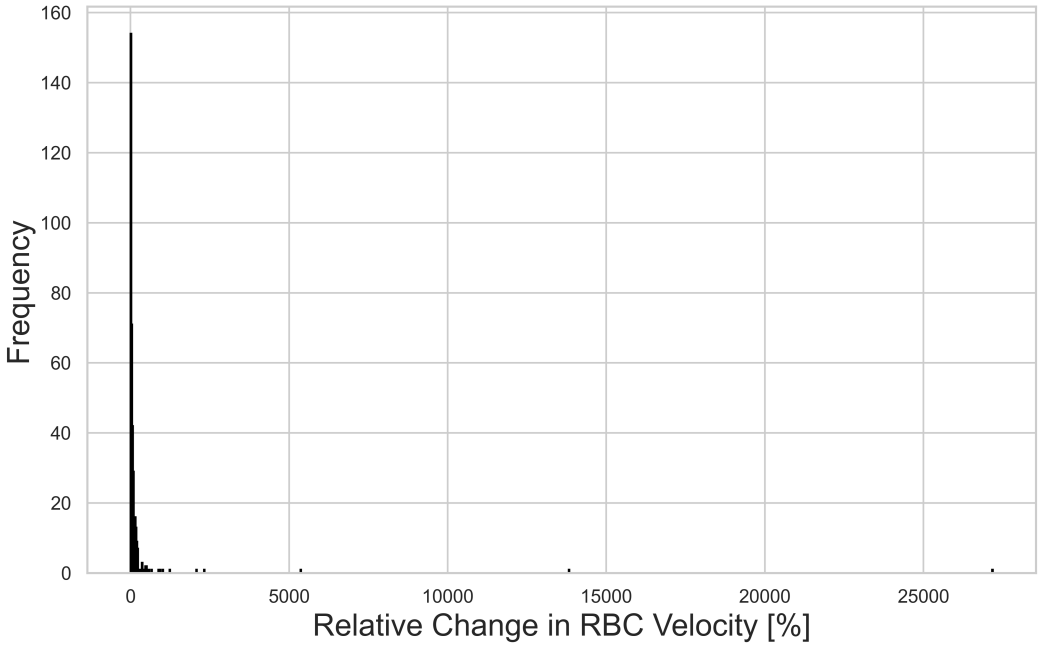

Figure 45: RBC velocity relative change comparing Baseline and stroke histogram.

8. Discussion

To conclude this work, it is important to highlight, summarize, and explain the results obtained and presented in the previous sections. However, it is crucial to consider the limitations of the project for a proper evaluation of these results. Understanding these limitations will provide better insight into the reasons behind the obtained results and their significance.

1. The solution of changing the cost function and simulating sequentially to obtain physiological values of red blood cell velocity, pressure difference, CBF, etc., could still be improved. Despite improving the results, there is still room for improvement, especially in the case where the microstroke is induced.

2. It is important to acknowledge the possibility of errors in the extraction of the network and experimental measurements, both of which introduce uncertainties into the analysis. These uncertainties can significantly impact the results obtained and the key challenge of this study is to reduce the uncertainty as much as possible. In fact, as observed, two measurements were excluded due to errors in problematic areas of the network. This underscores the importance of careful validation and verification processes to ensure the accuracy and reliability of the data used in the study.

3. In all simulations, a constant haematocrit throughout the network is assumed. However, in reality, this is not the case, and it would be better to implement a method for tracking red blood cells with a bifurcation rule. This could alter the distribution of red blood cells obtained and the overall flow in the network. It could also help with obtaining a good solution from the inverse model.

Before the final study with the obtained vascular network and experimental measurements, the insights gained from the preliminary study were crucial.

Based on the obtained results, it is evident that the second method proposed for inducing occlusion appears to be invalid. The reduction in diameter of the blocked edge without tuning again the boundary conditions leads to significant alterations in the flow field, with no discernible trend observed with respect to the generations or bifurcation types. This inconsistency, coupled with relatively large changes in boundary conditions when not tuned, suggests that the first method, involving tuned boundary conditions, is more suitable for inducing microstroke in the final study. Additionally, while tuning the boundary conditions successfully induced the microstroke, it is noted that using the same velocities as the baseline simulation as target values may slightly affect the results, potentially leading to changes in flow rates in other vessels in the network.

Furthermore, analysis of the pressure changes at boundary conditions relative to the distance from the stroke reveals a strong correlation, with greater changes observed closer to the microstroke. However, it is important to consider a distance referenced to the network rather than Euclidean distance for more accurate assessments. Despite the noticeable pressure changes near the microstroke, they are not substantial, and outliers with significant changes are observed further from the blocked capillary. This discrepancy suggests a need to account

for flow direction when calculating distances between the microstroke and each boundary, enhancing the precision of future studies.

When inducing the stroke in the final study, a significant increase in the pressure difference across the network can be observed. This may be due to what was observed in the preliminary study: the pressure value of some boundary conditions near the occlusion changes significantly because the blocked capillary is located quite close to the edge of the network. This can even cause a boundary condition that was an outflow under healthy conditions to become an inflow under blockage conditions, or vice versa. This also explains why the CBF in the case with a stroke is slightly higher than in the healthy case, as more blood is entering the network with the blocked capillary than without it.

As explained earlier, out of the 38 directional changes that occur when inducing the stroke, only 2 happen in the generations close to the blocked capillary. There is a possibility that there are fewer directional changes in reality, but due to the lack of measurements in other regions of the network, there will always be some uncertainty. Therefore, we should focus on how the flow redistributes around the occlusion.

Due to the mentioned limitations, there are several aspects where the work remains incomplete:

1. Analyzing the network to identify potential issues that may have arisen during its creation and verifying whether the two excluded experimental measurements were indeed the cause of the problems. This would help reduce result uncertainty by using the maximum number of experimentally obtained velocities.

2. Simulating the two time points after the stroke: 2 hours post-stroke and 24 hours post-stroke to fully analyze the flow evolution after the occlusion and evaluate its consequences, especially regarding oxygen transport by red blood cells in the affected area.

3. As observed, the type of bifurcation where the occlusion occurs has a significant influence on how the flow redistributes. In this study, the occlusion is induced in a single capillary, and therefore it would be optimal to have at least one case for each type of bifurcation. Additionally, the location where the stroke is induced is quite close to the border of the network, which may result in excessive changes in the pressure of the nearby boundary conditions. This highlights the importance of considering the location and type of occlusion [16] when designing future studies to better understand the effects on flow redistribution and pressure changes in vascular networks.

Additionally, there are several aspects that need improvement:

1. Acounting for the presence of RBC by tracking them through the network leads to a varying haematocrit field and impacts the flow field.

2. To find another solution to achieve more physiological results without such a significant change in pressure once the microstroke is induced. To address this, instead of employing a constraint on RBC velocity for all vessels in the network, one approach could be to directly implement a method that restricts the percentage change in pressure for

each boundary, depending on the type of blood vessel (artery, vein, or capillary). Another potential solution could involve utilizing a regulation mechanism based on CBF. By incorporating these strategies, it may be possible to achieve more precise control over the simulation parameters, enhancing the accuracy and reliability of the results.

References

[1] D G Altman and J M Bland. "Statistics Notes: Quartiles, quintiles, centiles, and other quantiles". In: *BMJ* 309.6960 (Oct. 15, 1994), pp. 996–996. ISSN: 0959-8138, 1468-5833. DOI: 10.1136/bmj.309.6960.996. URL: https://www.bmj.com/lookup/doi/10.1136/bmj.309.6960.996 (visited on 03/17/2024).

[2] Oguz K Baskurt. "Blood Rheology and Hemodynamics". In: *SEMINARS IN THROMBOSIS AND HEMOSTASIS* 29.5 (2003).

[3] Pablo Blinder et al. "The cortical angiome: an interconnected vascular network with noncolumnar patterns of blood flow". In: *Nature Neuroscience* 16.7 (July 2013), pp. 889–897. ISSN: 1097-6256, 1546-1726. DOI: 10.1038/nn.3426. URL: https://www.nature.com/articles/nn.3426 (visited on 02/20/2024).

[4] Clément Brunner. "Université Paris Descartes, Sorbonne Paris Cité Ecole Doctorale Cerveau, Cognition, Comportement". Thèse pour l'obtention du grade de Docteur en Neurosciences. PhD Thesis. Université Paris Descartes, Sorbonne Paris Cité, 2023.

[5] W. R. Dean. "Fluid Motion in a Curved Channel". In: *Proceedings of the Royal Society of London. Series A* 122 (1927), pp. 402–420.

[6] Robert Epp. "Inverse model for biphasic blood flow in the microcirculation". In: (2023). Diss. ETH No. 28975.

[7] Robert Epp, Franca Schmid, and Patrick Jenny. "Hierarchical regularization of solution ambiguity in underdetermined inverse and optimization problems". In: *Journal of Computational Physics: X* 13 (Jan. 2022), p. 100105. ISSN: 25900552. DOI: 10.1016/j.jcpx.2022.100105. URL: https://linkinghub.elsevier.com/retrieve/pii/S2590055222000014 (visited on 02/20/2024).

[8] Robert Epp et al. "Predicting Vessel Diameter Changes to Up-Regulate Biphasic Blood Flow During Activation in Realistic Microvascular Networks". In: *Frontiers in Physiology* 11 (Oct. 16, 2020), p. 566303. ISSN: 1664-042X. DOI: 10.3389/fphys.2020.566303. URL: https://www.frontiersin.org/article/10.3389/fphys.2020.566303/full (visited on 02/20/2024).

[9] Robin Fåhræus and Torsten Lindqvist. "THE VISCOSITY OF THE BLOOD IN NARROW CAPILLARY TUBES". In: *American Journal of Physiology-Legacy Content* 96.3 (Mar. 1, 1931), pp. 562–568. ISSN: 0002-9513. DOI: 10.1152/ajplegacy.1931.96.3.562. URL: https://www.physiology.org/doi/10.1152/ajplegacy.1931.96.3.562 (visited on 03/17/2024).

[10] Dmitry A. Fedosov et al. "Blood Flow and Cell-Free Layer in Microvessels: Blood Flow and Cell-Free Layer in Microvessels". In: *Microcirculation* 17.8 (Nov. 2010), pp. 615–628. ISSN: 10739688. DOI: 10.1111/j.1549-8719.2010.00056.x. URL: https://onlinelibrary.wiley.com/doi/10.1111/j.1549-8719.2010.00056.x (visited on 03/17/2024).

[11] Saad Hikmat Haji and Adnan Mohsin Abdulazeez. "COMPARISON OF OPTIMIZATION TECHNIQUES BASED ON GRADIENT DESCENT ALGORITHM: A REVIEW". In: (2021).

[12] N. A. Lassen and M. S. Christensen. "Physiology of Cerebral Blood Flow". In: *British Journal of Anaesthesia* 48 (1976), pp. 719–734.

[13] Maud Pétrault et al. "Cerebral microbleeds: Beyond the macroscope". In: *International Journal of Stroke* 14.5 (July 2019), pp. 468–475. ISSN: 1747-4930, 1747-4949. DOI: 10.1177/1747493019830594. URL: http://journals.sagepub.com/doi/10.1177/1747493019830594 (visited on 02/20/2024).

[14] A. R. Pries, D. Neuhaus, and P. Gaehtgens. "Blood viscosity in tube flow: dependence on diameter and hematocrit". In: *American Journal of Physiology-Heart and Circulatory Physiology* 263.6 (Dec. 1, 1992), H1770–H1778. ISSN: 0363-6135, 1522-1539. DOI: 10.1152/ajpheart.1992.263.6.H1770. URL: https://www.physiology.org/doi/10.1152/ajpheart.1992.263.6.H1770 (visited on 02/20/2024).

[15] A. R. Pries and T. W. Secomb. "Microvascular blood viscosity in vivo and the endothelial surface layer". In: *American Journal of Physiology-Heart and Circulatory Physiology* 289.6 (Dec. 2005), H2657–H2664. ISSN: 0363-6135, 1522-1539. DOI: 10.1152/ajpheart.00297.2005. URL: https://www.physiology.org/doi/10.1152/ajpheart.00297.2005 (visited on 02/20/2024).

[16] Franca Schmid et al. "Depth-dependent flow and pressure characteristics in cortical microvascular networks". In: *PLOS Computational Biology* 13.2 (Feb. 14, 2017). Ed. by Jeffrey J. Saucerman, e1005392. ISSN: 1553-7358. DOI: 10.1371/journal.pcbi.1005392. URL: https://dx.plos.org/10.1371/journal.pcbi.1005392 (visited on 02/20/2024).

[17] Franca Schmid et al. "Red blood cells stabilize flow in brain microvascular networks". In: *PLOS Computational Biology* 15.8 (Aug. 30, 2019). Ed. by David Kleinfeld, e1007231. ISSN: 1553-7358. DOI: 10.1371/journal.pcbi.1007231. URL: https://dx.plos.org/10.1371/journal.pcbi.1007231 (visited on 02/20/2024).

[18] Franca Schmid et al. "The impact of capillary dilation on the distribution of red blood cells in artificial networks". In: *American Journal of Physiology-Heart and Circulatory Physiology* 308.7 (Apr. 1, 2015), H733–H742. ISSN: 0363-6135, 1522-1539. DOI: 10.1152/ajpheart.00335.2014. URL: https://www.physiology.org/doi/10.1152/ajpheart.00335.2014 (visited on 02/20/2024).

[19] Franca Schmid et al. "The severity of microstrokes depends on local vascular topology and baseline perfusion". In: *eLife* 10 (May 18, 2021), e60208. ISSN: 2050-084X. DOI: 10.7554/eLife.60208. URL: https://elifesciences.org/articles/60208 (visited on 02/20/2024).

[20] Timothy W. Secomb, Beata Styp-Rekowska, and Axel R. Pries. "Two-Dimensional Simulation of Red Blood Cell Deformation and Lateral Migration in Microvessels". In: *Annals of Biomedical Engineering* 35.5 (May 2007), pp. 755–765. ISSN: 0090-6964, 1573-9686. DOI: 10.1007/s10439-007-9275-0. URL: https://link.springer.com/10.1007/s10439-007-9275-0 (visited on 03/17/2024).

[21] Andy Y Shih et al. "The smallest stroke: occlusion of one penetrating vessel leads to infarction and a cognitive deficit". In: *Nature Neuroscience* 16.1 (Jan. 2013), pp. 55–63. ISSN: 1097-6256, 1546-1726. DOI: 10.1038/nn.3278. URL: https://www.nature.com/articles/nn.3278 (visited on 03/17/2024).

[22] Andy Y. Shih et al. "Rodent Models of Cerebral Microinfarct and Microhemorrhage". In: *Stroke* 49.3 (Mar. 2018), pp. 803–810. ISSN: 0039-2499, 1524-4628. DOI: 10.1161/STROKEAHA.117.016995. URL: https://www.ahajournals.org/doi/10.1161/STROKEAHA.117.016995 (visited on 02/20/2024).

[23] Mark W Siebert and Petru S Fodor. "Newtonian and Non-Newtonian Blood Flow over a Backward-Facing Step – A Case Study". In: *Proceedings of the COMSOL Conference 2009 Boston*. Cleveland State University. Cleveland, OH, 2009.

[24] Susanne J Van Veluw et al. "Detection, risk factors, and functional consequences of cerebral microinfarcts". In: *The Lancet Neurology* 16.9 (Sept. 2017), pp. 730–740. ISSN: 14744422. DOI: 10.1016/S1474-4422(17)30196-5. URL: https://linkinghub.elsevier.com/retrieve/pii/S1474442217301965 (visited on 02/20/2024).

[25] Susanne J Van Veluw et al. "In vivo characterization of spontaneous microhemorrhage formation in mice with cerebral amyloid angiopathy". In: *Journal of Cerebral Blood Flow & Metabolism* 41.1 (Jan. 2021), pp. 82–91. ISSN: 0271-678X, 1559-7016. DOI: 10.1177/0271678X19899377. URL: http://journals.sagepub.com/doi/10.1177/0271678X19899377 (visited on 02/20/2024).

[26] Zvonimir Vrselja et al. "Function of Circle of Willis". In: *Journal of Cerebral Blood Flow & Metabolism* 34.4 (Apr. 2014), pp. 578–584. ISSN: 0271-678X, 1559-7016. DOI: 10.1038/jcbfm.2014.7. URL: http://journals.sagepub.com/doi/10.1038/jcbfm.2014.7 (visited on 02/20/2024).

[27] Eric W. Weisstein. *Graph Distance Matrix*. https://mathworld.wolfram.com/GraphDistanceMatrix.html. Accessed: [2024-03-17]. n.d.

[28] Shuai Yang et al. "Diverse Functions and Mechanisms of Pericytes in Ischemic Stroke". In: *Current Neuropharmacology* 15.6 (July 31, 2017). ISSN: 1570159X. DOI: 10.2174/1570159X15666170112170226. URL: http://www.eurekaselect.com/149209/article (visited on 02/20/2024).

Appendix I: Budget

In this section, the overall budget for the completion of this work is presented. This budget is divided into the cost of human resources and the costs of computer equipment, computing, and software.

1. Human resources costs

In this project, various individuals participated, each dedicating a number of hours to the completion of the project. The cost of human resources is calculated in proportion to these hours spent. The master's thesis project consists of 12 ECTS, which corresponds to 30 hours each, totaling 360 hours. However, to carry out this project, a six-month stay at the ARTORG Center was required. Therefore, the total was 960 hours. This work required a significant number of hours for learning in the field of biomedical engineering and familiarization with the code used for the simulations. The hours were distributed as follows:

- Learning and familiarization with the code: 320h
- Preliminary study: 160h
- Final study: 320h
- Writing the thesis: 160h

The labor budget is thus presented in Table 15.

Table 15: Labor budget breakdown

Concept	**Time [h]**	**Wage (€/h)**	**Value [€]**
Author	960	14	13440
PhD Candidate I	100	25	2500
PhD Candidate II	100	25	2500
Supervisor	25	35	875
External Supervisor	50	50	2500
Total:	**21815 €**		

This expense amounts to a total of **TWENTY-ONE THOUSAND EIGHT HUNDRED AND FIFTEEN EUROS** (21815€).

2. Cost of computer equipment and software

For both the execution of all simulations as well as all pre-processing and post-processing, the personal computer was used, ROG Strix G513IC G513IC (processor: AMD Ryzen 7 4800H with Radeon Graphics, 2.90 GHz, installed RAM: 16.0 GB) The computer cost 1,400€ one year and three months ago. Assuming a depreciation of 20%, the current value of the computer is 1,050€. All simulations, pre-processing, and post-processing were performed on this computer.

The software used is open-source. Python was used to conduct the simulations, pre-processing, and post-processing, while ParaView was also utilized for various aspects of pre-processing

and post-processing. Additionally, Overleaf was used for the drafting of the report.

Therefore, the only cost for this part is that of the personal computer, amounting to **THREE HUNDRED AND FIFTY EUROS** (350€).

3. Final budget

The total computation of costs is shown in Table 16.

Table 16: Overall Budget

Concept	**Value [€]**
Human Resources	21815
Computer Equipment and Software	350
Total	**22165**

The total cost of the project amounts to **TWENTY-TWO THOUSAND ONE HUNDRED AND SIXTY FIVE ERUOS** (22165€).

Appendix II: Sustainable Development Goals

Below, the degree of the work's alignment with the Sustainable Development Goals (SDGs) of the 2023 agenda is presented.

Table 17: Alignment of the Project with the Sustainable Development Goals (SDGs) of the 2023 Agenda

Sustainable Development Goals	**High**	**Medium**	**Low**	**Not Applicable**
SDG 1. No Poverty				X
SDG 2. Zero Hunger				X
SDG 3. Health and Well-being	X			X
SDG 4. Quality Education				X
SDG 5. Gender Equality				X
SDG 6. Clean Water and Sanitation				X
SDG 7. Affordable and Clean Energy				X
SDG 8. Decent Work and Economic Growth				X
SDG 9. Industry, Innovation and Infrastructure				X
SDG 10. Reduced Inequalities				X
SDG 11. Sustainable Cities and Communities				X
SDG 12. Responsible Consumption and Production				X
SDG 13. Climate Action				X
SDG 14. Life Below Water				X
SDG 15. Life on Land				X
SDG 16. Peace, Justice, and Strong Institutions				X
SDG 17. Partnerships for the Goals				X

Given the focus of this project on the understanding on how microstrokes affect blood flow around the occlusion, the following SDG is considered:

SDG 3: Health and Well-being: The study of the microstrokes contributes to the understanding on why the accumulation throughout the lifetime of a person of these occlusions causes dementia. Understanding why the disease occurs is the first step towards being able to prevent it.